Martian atmospheric collapse: Idealized GCM studies

Alejandro Soto [a,b,*], Michael Mischna [c], Tapio Schneider [d,e], Christopher Lee [f], Mark Richardson [f]

[a] Division of Geological and Planetary Sciences, California Institute of Technology, Pasadena, CA 91125, USA
[b] Southwest Research Institute, Boulder, CO 80302, USA
[c] Jet Propulsion Laboratory, California Institute of Technology, Pasadena, CA 91109, USA
[d] Department of Earth Sciences, ETH Zurich, Switzerland
[e] Environmental Science and Engineering, California Institute of Technology, Pasadena, CA 91125, USA
[f] Ashima Research, Pasadena, CA 91106, USA

ARTICLE INFO

ABSTRACT

Global energy balance models of the martian atmosphere predict that, for a range of total CO_2 inventories, the CO_2 atmosphere may condense until a state with a permanent polar cap is reached. This process, which is commonly referred to as atmospheric collapse, may limit the time available for physical and chemical weathering. The global energy balance models that predict atmospheric collapse represent the climate using simplified parameterizations for atmospheric processes such as radiative transfer and atmospheric heat transport. However, a more detailed representation of these atmospheric processes is critical when the atmosphere is near a transition, such as the threshold for collapse. Therefore, we use the Mars Weather Research and Forecasting (MarsWRF) general circulation model (GCM) to investigate how the explicit representation of meridional heat transport and more detailed radiative transfer affects the onset of atmospheric collapse. Using MarsWRF, we find that previous energy balance modeling underestimates the range of CO_2 inventories for which the atmosphere collapses and that the obliquity of Mars determines the range of CO_2 inventories that can collapse. For a much larger range of CO_2 inventories than expected, atmospheric heat transport is insufficient to prevent the atmospheric collapse. We show that the condensation of CO_2 onto Olympus Mons and adjacent mountains generates a condensation flow. This condensation flow syphons energy that would otherwise be transported poleward, which helps explain the large range of CO_2 inventories for which the atmosphere collapses.

1. Introduction

An important constraint on the evolution of the martian atmosphere is the partitioning of the martian CO_2 inventory between the atmosphere and the surface. When the solar and thermal energy that arrives at the surface of Mars is low enough, the resulting surface temperature can be below the sublimation temperature of CO_2 (Leighton and Murray, 1966). The atmosphere then completely deposits its CO_2 onto the surface, which is sometimes called "atmospheric collapse", until the atmosphere achieves a thermodynamic balance between the atmosphere and surface reservoirs of CO_2 (Leighton and Murray, 1966; Gierasch and Toon, 1973; McKay et al., 1991; Haberle et al., 1994; Nakamura and Tajika, 2002). Thus, three martian climates are possible: a climate free of surface CO_2 ice, a climate with CO_2 surface ice in thermodynamic balance with the atmosphere (a "collapsed atmosphere"), and a transitional climate undergoing atmospheric collapse.

If atmospheric collapse indeed occurs, it is important for understanding the geological history of Mars and needs to be considered as part of its geological history, which already includes water ice ages on Mars (Head et al., 2003). A standard geological paradigm for the history of Mars requires a thick atmosphere, of a few hundred millibars global-mean surface pressure or greater, to create periods of warm and wet near-surface conditions through much of the Noachian (4.1–3.7 billion years ago), and at least episodic periods of warmth since that time to form valley systems that are a geomorphic hallmark of surface water flow (Andrews-Hanna and Lewis, 2011; Carr and Head, 2010; Fassett and Head, 2011; Grotzinger et al., 2005; Ehlmann et al., 2011; Mischna et al., 2013). Any collapse of the atmosphere would have placed limits on the duration of warm climates (Haberle et al., 1994).

The extant global-mean climate models that predict atmospheric collapse (e.g. Haberle et al., 1994; Manning et al., 2006) use a simplified representation of radiative transfer to calculate

local radiative heating. They represent the atmospheric heat transport, which is an inherently three-dimensional and time varying process, in terms of a single 'constant' flux. But simplified radiative transfer calculations fail to correctly simulate the greenhouse effect of CO_2-dominant atmospheres, like the one on Mars, thus requiring more sophisticated calculations of radiative transfer (Halevy et al., 2009; Wordsworth et al., 2010). Using a single constant to represent the atmospheric heat transport is the weakest link in any low-order (zero-dimensional and one-dimensional) atmospheric evolution model, since the proper representation of heat transport is of critical importance when the atmosphere is near a transition, such as the threshold for collapse (Gierasch and Toon, 1973; Haberle et al., 1994). Because of these limitations in previous global-mean climate models, a higher-dimensional model is needed to understand the climate dynamics of atmospheric collapse, (Haberle et al., 1994).

Here we investigate the onset of atmospheric collapse using a three-dimensional general circulation model (GCM). Our GCM includes the full transport equations and a sophisticated treatment of the thermodynamics and radiative transfer of CO_2. Since our investigation focuses on the basic physical processes of atmospheric collapse, we have chosen to omit both dust and trace gas processes from our simulations for this initial investigation, as well as use the current solar luminosity to force the atmosphere. The goal of our investigation is to explore the climate processes involved in atmospheric collapse, not to simulate the climate history of Mars in detail. In particular, we investigate how the relationship between the polar surface temperature and surface pressure as predicted by the global-mean climate models differs from that predicted by the GCM. We then propose a physical process that accounts for the difference.

2. Conceptual model

Early investigations into martian atmospheric collapse used energy balance models (EBMs) to investigate the relationship between polar surface temperatures and the sublimation temperature (Leighton and Murray, 1966; Gierasch and Toon, 1973; McKay et al., 1991; Haberle et al., 1994; Nakamura and Tajika, 2002). These EBMs calculated the surface temperature by balancing the incoming and outgoing energy. Various climate feedbacks were incorporated in these models (Leighton and Murray, 1966; McKay et al., 1991; Nakamura and Tajika, 2002), and a few of theses models incorporated parameterizations of energy transport by atmospheric dynamics (Gierasch and Toon, 1973; Haberle et al., 1994). The results of these previous investigations describe a relationship between the polar surface temperature and the condensation of the atmospheric CO_2.

Fig. 1 conceptually shows this relationship by comparing the CO_2 condensation[1] curve to the polar surface temperature for a range of atmospheric surface pressures. The solid line in Fig. 1 is the condensation temperature as a function of surface pressure, as described by the Clausius–Clapeyron relation for CO_2 (Glasser, 2002). The dashed line is the polar surface temperature as a function of atmospheric surface pressure for a specific solar luminosity; this is the polar temperature that the energy balance generates before any CO_2 condensation generates latent heating. At both high surface pressure (i.e., above point B in Fig. 1) and low surface pressure (i.e., at or below point A) the polar surface temperature is above the condensation temperature such that all CO_2 is in the atmosphere and there are no permanent polar CO_2 ice caps. Point A is a stable
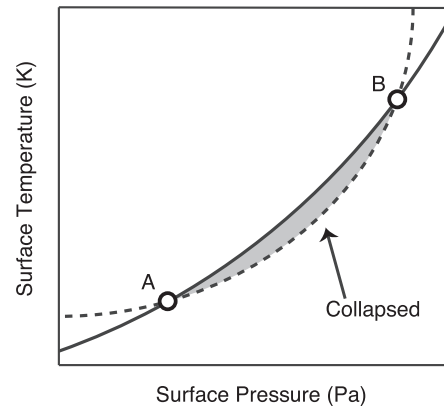

Fig. 1. A conceptual model of the relationship between polar surface temperature and CO_2 sublimation temperature. The solid black line represents the CO_2 sublimation curve. The dashed black line represents the annual mean polar surface temperature assuming atmospheric heat transport and a greenhouse effect. Point A and B are the transition points between a non-collapsed atmosphere and a collapsed atmosphere (gray region). Point A is a stable equilibrium point; point B is an unstable equilibrium point.

equilibrium point. A climate with sufficient CO_2 inventory and with a surface pressure below point A will continue to convert CO_2 ice into CO_2 gas until its surface pressure equals point A, where it will be in equilibrium. Likewise, a climate with a surface pressure above point A and below point B will condense its atmospheric CO_2 until it reaches the surface pressure of point A. Point B, however, is an unstable equilibrium point. Atmospheres with surface pressure below point B will condense until the surface pressure reaches point A. During this process, the martian climate is experiencing atmospheric collapse, which we define as the presence and multi-year secular growth of at least one permanent CO_2 ice cap. Atmospheres above point B will not collapse and have no permanent CO_2 ice caps. Thus, the martian atmosphere can experience two types of stable climates: first, an inflated, CO_2 ice-free climate that occurs above point B or below point A in Fig. 1; and second, a vapor pressure balanced climate where atmospheric CO_2 and surface CO_2 ice stably co-exist at point A. All other types of climate are transitory.

Using the relationship between polar surface temperature and CO_2 condensation shown in Fig. 1, Haberle et al. (1994) found that early in martian history, and for a range of initial total CO_2 inventories, the atmosphere would be unable to stave off year-round CO_2 polar caps. Additionally, Manning et al. (2006) found that obliquity variations created cycles of atmospheric collapse and non-collapse throughout martian history. If Mars were trapped in a collapsed state for extended periods of its planetary history, the amount of time available for physical and chemical weathering would, as a result, be greatly limited. Therefore, an accurate representation of the relationship between polar surface temperature and CO_2 condensation is a vital input into any modeling of the evolution of the martian climate (Haberle et al., 1994; Manning et al., 2006).

3. Using a general circulation model

Previous studies of atmospheric collapse on Mars used EBMs of varying forms and spatial dimensions to investigate both the climate dynamics and the evolution of atmospheric collapse (Gierasch and Toon, 1973; McKay et al., 1991; Haberle et al., 1994; Manning et al., 2006; Nakamura and Tajika, 2002). These EBMs are of appropriate complexity for early investigations into the collapse phenomena, and they have provided insight into the stability and instability of the martian atmosphere. To increase our understanding of the physics of collapse and to improve our

---

[1] Although the phase transition of CO_2 from gas to solid is properly called 'deposition', we use the term 'condensation' in order to be consistent with previous Mars literature (e.g. Pollack et al. (1990), Haberle et al. (1994), and Forget et al. (2013)).

predictions of which climate states lead to collapse, we require a climate model that includes a more detailed and complete representation of atmospheric processes. Two physical processes are of particular concern: radiative transfer through the CO_2 atmosphere and the meridional transport of heat. For our study, these two processes must be accurately captured for a large range of global-mean surface pressures. To meet these requirements, we use the MarsWRF general circulation model (GCM) of the martian atmosphere. We discuss the details of our model in the following section, but first we provide some justifications for using this GCM.

EBMs generally calculate the radiative transfer by assuming a single-layer gray atmosphere. Although the details vary from model to model, the basic setup is the same: assume that the atmosphere acts as a gray body that absorbs uniformly at all wavelengths and calculate the energy balance at the top of the atmosphere and at the surface. The coefficients in the radiative transfer equations are then set to match the predominant atmospheric gas involved in the radiative transfer process, which on Mars is CO_2. Although these types of radiative transfer calculations are useful in initial climate investigations, we know from prior investigations that the gray atmosphere approximation does not accurately reproduce the atmospheric radiative transfer (Goody and Yung, 1989). For example, gray models cannot easily capture how atmospheric radiative transfer changes with surface pressure, going from Lorentzian absorption to 'collision-induced absorption' (CIA) (Halevy et al., 2009; Wordsworth et al., 2010). This is a phenomenon that has been extensively studied in the Earth's atmosphere and that is applicable to the martian atmosphere (Halevy et al., 2009; Wordsworth et al., 2010; Mischna et al., 2012). Mischna et al. (2012) have developed a k-distribution radiative transfer scheme for MarsWRF that addresses the challenges in calculating radiative transfer for a thick CO_2 atmosphere. This radiative transfer scheme is described in the following section; details of the scheme are provided by Mischna et al. (2012).

By transporting heat from the tropics to the polar regions, meridional heat transport contributes to the polar energy balance that determines polar air and surface temperatures (Gierasch and Toon, 1973; Lindzen and Farrell, 1977, 1980; Peixoto and Oort, 1992; Haberle et al., 1994; Pierrehumbert, 2010). The transport of heat also helps determine if ice forms from volatiles in the atmosphere (Gierasch and Toon, 1973; Lindzen and Farrell, 1977, 1980; Haberle et al., 1994). Even in a thin atmosphere, like the current martian atmosphere, where any given atmospheric column is near local radiative–convective equilibrium, meridional heat transport still influences the formation of ice by changing the atmospheric temperature over long periods of time (Pierrehumbert, 2010). Therefore, to correctly simulate the polar climate of Mars, any climate modeling of Mars must include an accurate representation of meridional heat transport.

Some of the EBMs previously used to study atmospheric collapse on Mars used parameterizations for the meridional heat transport (Gierasch and Toon, 1973; Haberle et al., 1994; Manning et al., 2006). These parameterizations were originally derived by Stone (1972) for climate studies of the Earth, assuming that the maximum meridional heat transport is due to dry baroclinic eddies in the mid-latitudes. However, the assumption that meridional heat transport on Mars is determined by midlatitude baroclinic eddies may not be valid, as mean meridional circulations and stationary eddies may also play a role (Gierasch and Toon, 1973; Lindzen and Farrell, 1980; Haberle et al., 1994). The use of a GCM ameliorates this problem by explicitly solving the transport equations.

By using a three dimensional general circulation model (GCM), we are able to study the response of the martian paleoclimate CO_2 cycle to different forcing scenarios over diurnal, seasonal, and annual time frames. We focus on the relationships between CO_2

inventory, obliquity, and planetary energy balance in controlling the partition of CO_2 between the atmosphere and the surface. The regolith reservoir and atmospheric loss are omitted from our model, since any changes to the CO_2 concentration in the regolith or the CO_2 loss rate to space are negligible on the time scale of our simulations.

Forget et al. (2013) and Kahre et al. (2013) have both explored the effects of atmospheric collapse on the possible climate states of ancient Mars. As part of a larger study that investigated the possible mechanisms for warming an ancient Mars under a dimmer Sun, Forget et al. (2013) identified the paleoclimate conditions for atmospheric collapse for a range of surface pressures and obliquities and included the effects of radiatively active clouds and atmospheric dust. Kahre et al. (2013) focused on how dust loading may determine whether the ancient martian climate was in a collapsed or un-collapsed state. Additionally, Kahre et al. (2013) investigated how the ability of dust loading to stabilize the martian atmosphere depends on the CO_2 ice albedo and obliquity of Mars. Our investigation does not directly address this recent research. Instead, we are focusing on understanding the dynamical mechanisms that control atmospheric collapse. Additionally, we have chosen to focus on the current solar luminosity, which allow us to compare the results from our thin atmosphere simulations to current Mars. In a future paper we will address the dynamics of atmospheric collapse in the ancient martian climate due to a lower-luminosity Sun, as well as compare our results to the results of Forget et al. (2013) and Kahre et al. (2013).

4. Model and simulations

We used the Mars Weather Research and Forecasting (Mars-WRF) GCM, a generalized, planetary version of the NCAR Weather Research and Forecasting (WRF) model (Skamarock et al., 2005; Richardson et al., 2007; Toigo et al., 2012). For this investigation, we used version 3.0.1.2 of MarsWRF. The model compares well to other martian GCMs (see, e.g., Section 4 in Richardson et al. (2007)). MarsWRF solves the primitive equations on a finite difference mesh using an Arakawa C-grid. As described in Richardson et al. (2007), the model calculates CO_2 sublimation and deposition and then adjusts the CO_2 ice and atmosphere inventories, along with the column mass and pressure, accordingly. Although dust and water vapor would affect the heating and temperature profile in our model, we do not include dust or water vapor in our simulations in order to focus on the climate dynamics of a CO_2 atmosphere. The contribution of dust and water vapor may be limited in any case (Wordsworth et al., 2013; Forget et al., 2013; Kahre et al., 2013; Urata and Toon, 2013). Simulations are run with a latitude and longitude resolution of $5° \times 5°$ and with 40 vertical levels provided by a terrain-following vertical sigma coordinate (Laprise, 1992; Skamarock et al., 2008). We do not include a CO_2 cloud scheme. For our work, this is a reasonable choice since it is not clear whether CO_2 clouds would warm or cool the atmosphere (Forget and Pierrehumbert, 1997; Mischna et al., 2000; Colaprete and Toon, 2003). For surface temperature calculations, a multilayer subsurface thermal diffusion and surface energy balance model uses surface albedo and thermal inertia maps derived from orbital observations of the martian surface by the Thermal Emission Spectrometer (TES) on the Mars Global Surveyor (Christensen et al., 2001; Putzig et al., 2005). The version of MarsWRF used here includes a high resolution MOLA topography map, down-sampled to the $5° \times 5°$ horizontal resolution of our simulations (Smith et al., 2001). At locations where surface CO_2 ice is present, the model sets the surface albedo to 0.6 and the surface emissivity to 0.8. No subsurface storage of CO_2 is considered, making our total CO_2 budget equal to the atmosphere plus cap amounts.

For radiation calculations, we use a two-stream radiation code that implements a k-distribution radiative transfer scheme (Mischna et al., 2012). The radiative transfer scheme divides the spectrum into 14 bins that span the visibile and infrared spectrum from 0.24 to 1000 μm. Seven of the bands are in the visible and seven of the bands are in the infrared. To account for the non-Lorentzian shape of the absorption lines, the scheme uses an empirical scaling provided by Perrin and Hartmann (1989) and suggested by Wordsworth et al. (2010). To account for collision induced absorption, the scheme uses an adjustment proposed by Halevy et al. (2009). Mischna et al. (2012) provides a detailed discussion of the k-distribution radiative transfer scheme used in this paper. Most importantly, this scheme was designed specifically for studies of thick atmospheres on Mars (Mischna et al., 2012).

We designed a suite of MarsWRF simulations to focus on two key parameters that affect the atmosphere's response to the polar energy balance: the total CO_2 inventory and the obliquity of Mars. These two parameters directly affect the greenhouse warming and the magnitude of insolation. Although other factors may influence the conditions for atmospheric collapse, such as variations in surface properties, the decameter-scale slopes (Kreslavsky and Head, 2005), the amount of atmospheric dust (Davies, 1979; Haberle et al., 1982; Forget et al., 2013; Kahre et al., 2013), and the orbital eccentricity (Laskar et al., 2004), the CO_2 inventory and the martian obliquity likely exert the largest influence on the local energy balance for a given solar luminosity, and in any case we want to understand this simpler system before layering on complexity. The changing luminosity of the Sun over the lifetime of the Solar System also controls the local energy balance (Gough, 1981; Gilliland, 1989). For this study, however, we chose to only simulate the current solar luminosity. The results of this study will allow us to later investigate how the changing luminosity affects atmospheric collapse. The purpose of the paper is to explore climate processes, not to reproduce the climate history of Mars in detail. Therefore, we simulated idealized climates that provide insight into the climate dynamics of atmospheric collapse.

To understand how the threshold of atmospheric collapse depends on the greenhouse warming strength, or lack thereof, we ran simulations for a variety of total CO_2 inventories. Each simulation has a total CO_2 inventory that corresponds to the equivalent mean surface pressure that the simulation would have if all of the CO_2 was in the atmosphere. Since our goal is to understand how the relationship between the polar surface temperature and surface pressure as predicted by EBMs differ from the relationship predicted by a GCM, we chose the range of CO_2 inventories, shown in Table 1 to encompass the same range used in previous EBM studies, including Haberle et al. (1994) and Manning et al. (2006).

Changes in the orbital parameters of Mars generate significant changes in the latitudinal distribution of insolation on the surface (Ward, 1974; Laskar et al., 2004). As we mentioned above, we are focusing on the obliquity variations in the orbital parameters. To do so, we set eccentricity, e, to zero in all of the simulations. Therefore, there will be no variation in the magnitude of the insolation

throughout the martian year due to the eccentricity or precession (Ward, 1974; Laskar et al., 2004). The obliquity, ε, influences the collapse criteria for the atmosphere by changing the latitudinal distribution of incident solar radiation (Ward, 1974; Laskar et al., 2004). Laskar et al. (2004) showed that statistical models of the 5 billion year evolution of the martian orbit generate an obliquity range of $\varepsilon = \sim 0°$ to $\varepsilon = \sim 80°$. Thus, it is possible that Mars spent some part of its history with an obliquity less than 20° and possibly as low as 0°. For our investigation, we ran simulations with obliquities from 0° to 45° in steps of 5°. As we show below, we did not simulate the climate at higher obliquities because atmospheric collapse no longer occurs for all CO_2 inventories at obliquities of 45° and higher for the current luminosity.

We ran more than 60 simulations covering a range of CO_2 inventories for each obliquity. Each simulation was initialized with a particular CO_2 inventory from Table 1, where all of the CO_2 was in the atmosphere, and with a particular obliquity. The simulations were run for at least 10 Mars years. We concluded from all of these long simulations that after four years the climate system reaches a "quasi-steady state", in both collapsing and non-collapsing atmospheres; therefore, we only show the first four years of simulation results in the figures below.

5. Results

The rate and location of CO_2 ice deposition are diagnostic of the polar energy balance that controls atmospheric collapse.[2] Fig. 2 shows the evolution of various atmospheres with different initial CO_2 inventories and the indicated obliquity, ε. The simulations include total CO_2 inventories of 6 mb, 60 mb, 300 mb, 600 mb, 1200 mb, and 3000 mb. The fraction of global CO_2 ice to the total global CO_2 in the simulation is plotted as a function of time. As CO_2 ice is deposited in the polar regions, the CO_2 ice fraction increases.

In all scenarios there is an initial period of rapid deposition of CO_2 ice as the surface energy balance equilibrates with the atmosphere, as seen in Fig. 2. After the initial half year, all of the simulations appear to settle into a steady pattern of either continuous collapse or seasonal exchange between the atmosphere and surface. In the zero obliquity ($\varepsilon = 0°$) simulations, all of the atmospheres are collapsing, since the atmospheric heating, including latent heat release from condensing CO_2, is insufficient to offset the cold temperatures at the permanently dark poles. As the obliquity increases in each successive plot in Fig. 2, a seasonal CO_2 ice cycle is convolved with the secular trend due to collapse. By $\varepsilon = 15°$ the seasonal cycle shows the semi-annual asymmetry that is due to the martian dichotomy and similar to pressure changes measured by the Viking Landers (Hess et al., 1980). Note that the seasonal cycles in these simulations do not exactly match the cycle seen in the Viking pressure curves since we have set eccentricity to zero.

The zonal-mean of surface CO_2 ice as a function of time shows the evolution of the CO_2 ice on the surface of Mars, as seen in Figs. 3–6. In each figure, the zonal-mean of the CO_2 ice is plotted against time for a total of five years. The plots capture both the seasonal surface deposition of CO_2 ice and the secular growth in CO_2 ice depth. The influence of topography on the CO_2 ice deposition is also apparent.

The atmospheric heating is insufficient to completely stop atmospheric collapse for obliquities of $\varepsilon = 15°$ or less, as shown in Figs. 3 and 4. In each of these simulations global CO_2 ice accumulation continues to increase with time, as the atmosphere slowly

Table 1

Simulations cover a wide range of possible atmospheric thicknesses. Each simulation starts with all of the CO_2 as gas. This table shows the range of CO_2 inventories simulated and the associated mass of CO_2 for each inventory.

Inventory name	Inventory mass (kg)
6 mb	0.028×10^{18}
60 mb	0.28×10^{18}
300 mb	1.4×10^{18}
600 mb	2.8×10^{18}
1200 mb	5.6×10^{18}
3000 mb	14.0×10^{18}

---

[2] For our investigation, we define the term "collapse" or "collapsed atmospheric state" as the presence of at least one permanent CO_2 ice cap, and the secular growth of this permanent cap over multiple years.
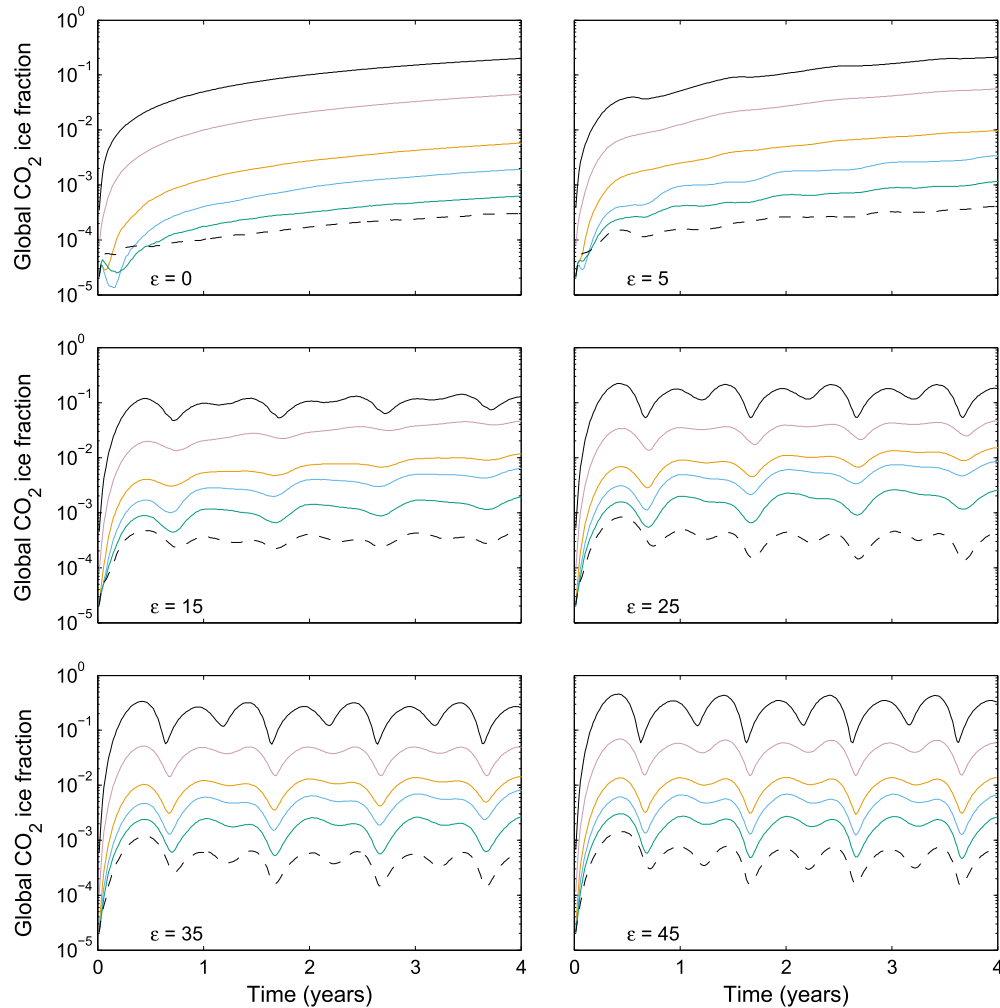
Fig. 2. Global accumulation of CO_2 ice for the various pressures at the indicated obliquity and zero eccentricity. The global CO_2 ice fraction is calculated as the ratio of the global sum of CO_2 surface ice to the total available CO_2. In all figures, each line represents a different initial CO_2 inventory: solid black = 6 mb, light red = 60 mb, orange = 300 mb, blue = 600 mb, green = 1200 mb, and dashed black = 3000 mb. (For interpretation of the references to color in this figure legend, the reader is referred to the web version of this article.)

condenses onto the polar surface. At $\varepsilon = 20°$ (not shown), however, two of the simulations cease to collapse: the 6 mb simulation and the 3000 mb simulation. In both of these 20° obliquity simulations, the atmosphere quickly achieves a state in which a fraction of the atmosphere exists as CO_2 ice on the surface, but there is no net annual increase in the accumulation of CO_2 ice after year two of the simulation. For the 6 mb simulation, the ice fraction stabilizes to around $\sim 10^{-1}$, and for the 3000 mb simulation the ice fraction stabilizes to $\sim 10^{-4}$, while the rest of the 20° obliquity simulations are still slowly collapsing. At higher obliquities, the mid-range atmospheric thicknesses continue to collapse while the ice fraction for the thickest and thinnest atmospheres no longer increases (Fig. 2). Finally, the 45° obliquity simulations are not collapsing, but instead display seasonal ice caps. By this obliquity, there is enough polar insolation and heat transport to stave off the collapse of the atmosphere.

In Fig. 3, which shows the zonal CO_2 ice versus time for $\varepsilon = 0°$, the CO_2 ice deposits preferentially on the north pole (although at low CO_2 inventories CO_2 ice deposits at both poles). This occurs because the topographically lower north pole has a higher surface pressure than the south pole, which leads to a higher sublimation temperature at the north pole. Generally, the north polar region of Mars should be more favorable to CO_2 condensation due to the Clausius–Clapeyron relation (Leighton and Murray, 1966). The

current martian atmosphere, however, has a perennial CO_2 polar cap at the south pole and only a seasonal CO_2 cap at the north pole (Kieffer et al., 1977; Kieffer, 1979). Various mechanisms have been proposed to explain this unexpected south polar preference for perennial CO_2 ice, including dust mixing with ice (Toon et al., 1980) and insolation dependent ice albedo changes (Wood and Paige, 1992). Since our CO_2 ice albedo value is constant and we are neglecting dust, our simulations will not correctly capture this south polar phenomenon. Because this phenomenon is not well understood, nor normally included in martian GCMs (Guo et al., 2010), we believe that this is the best assumption with which to proceed given our focus on understanding how atmospheric heat transport influences collapse.

As the CO_2 inventories increase in the $\varepsilon = 0°$ simulations in Fig. 3, from 6 mb to 3000 mb, there are two obvious shifts in the distribution of surface CO_2 ice. First, as mean global surface pressure increases, the south polar CO_2 ice cap disappears. By the 600 mb simulation, shown in Fig. 3(d), the southern perennial CO_2 ice cap no longer forms. For these larger CO_2 inventories, the increased greenhouse warming due to the increased CO_2 column mass and/or increased atmospheric transport outstrips the increasing condensation temperature due to increasing surface pressure for this pole. The south polar temperature set by surface pressure dependent greenhouse/advective heating is greater than the con-
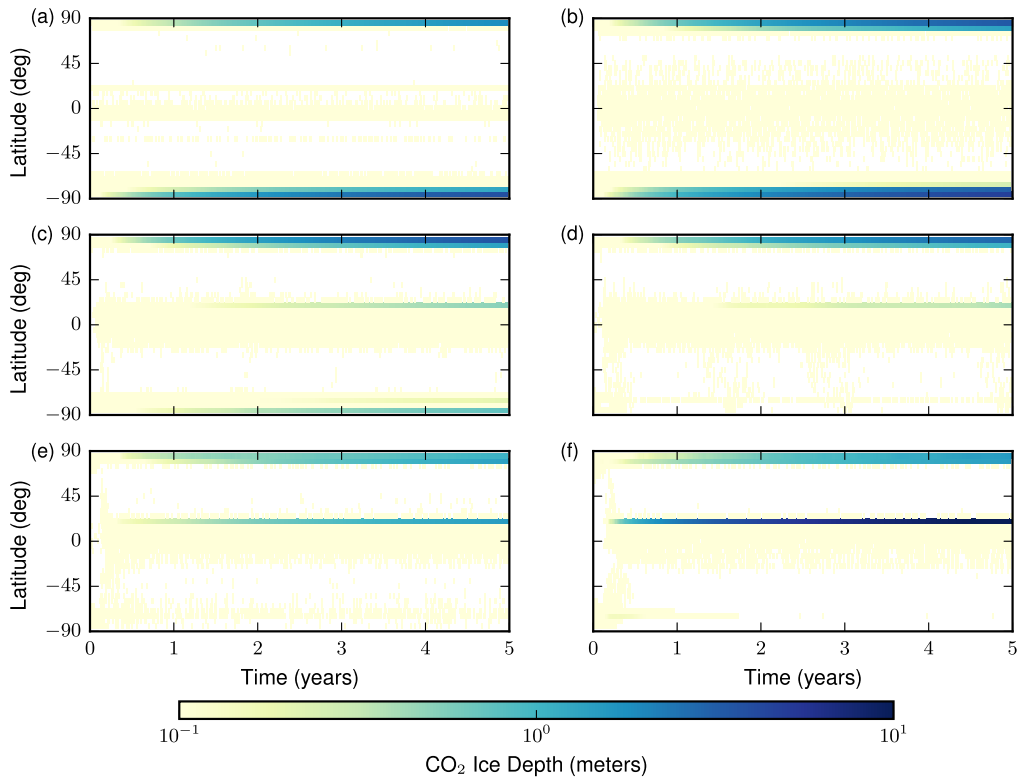
Fig. 3. Zonal CO$_2$ ice versus time for the current luminosity and the 0° obliquity. The plots include the following initial surface pressures: (a) 6 mb, (b) 60 mb, (c) 300 mb, (d) 600 mb, (e) 1200 mb, and (f) 3000 mb. The plots show the thickness of CO$_2$ ice assuming an ice density of 1600 kg/m^3. The band of accumulating CO$_2$ ice seen in the northern tropics is due to CO$_2$ condensation on Olympus Mons, as discussed in the text.
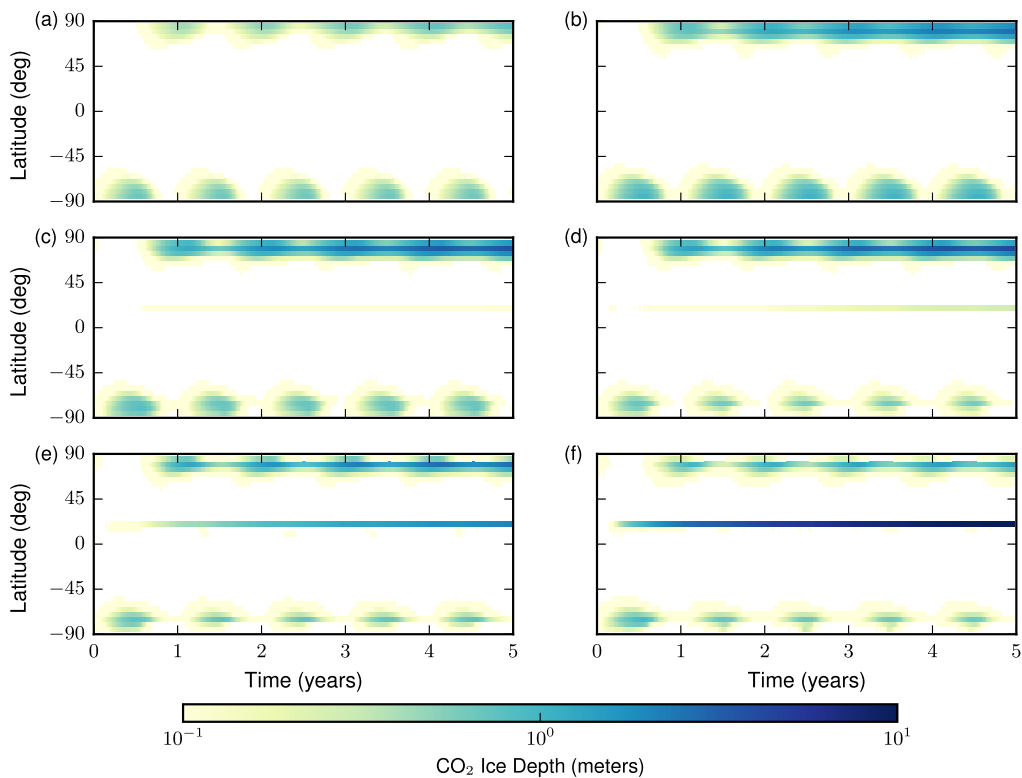

Fig. 4. Same as Fig. 3 but for 15° obliquity.

densation temperature provided by the Clausius–Clapeyron relation. If the simulation were run for a much longer period, the south polar surface pressure would decrease to the point where the south

polar surface temperature is below the CO$_2$ condensation temperature and the south polar CO$_2$ would form again. The second shift in CO$_2$ ice distribution is the deposition of CO$_2$ ice on the slopes of
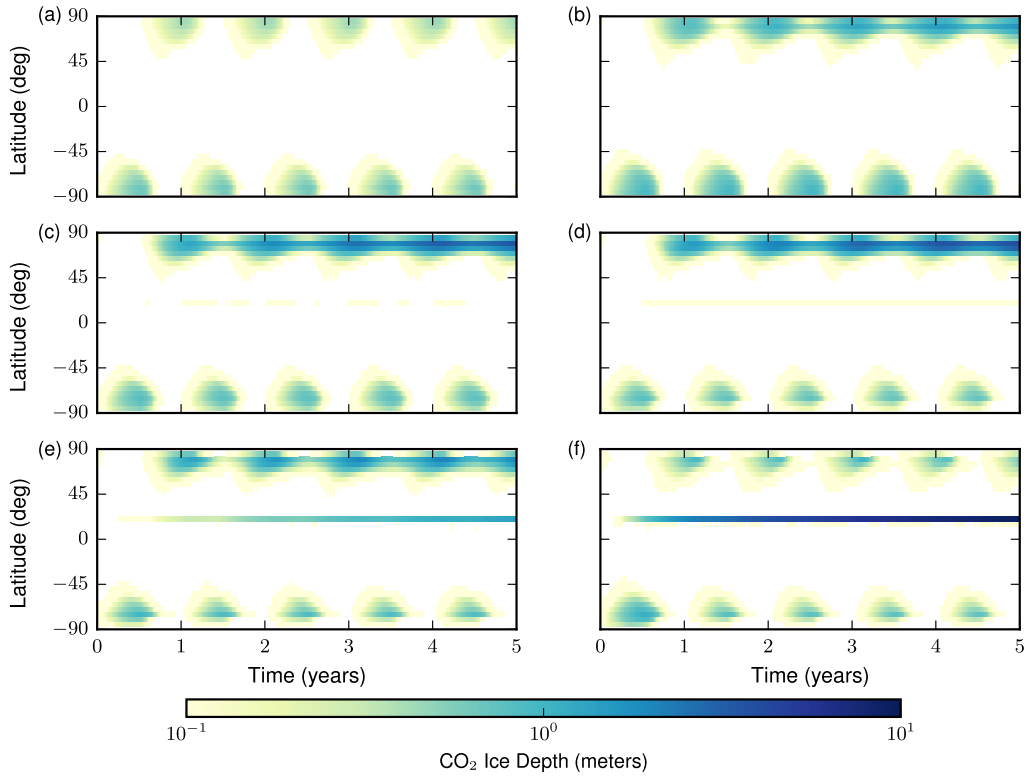
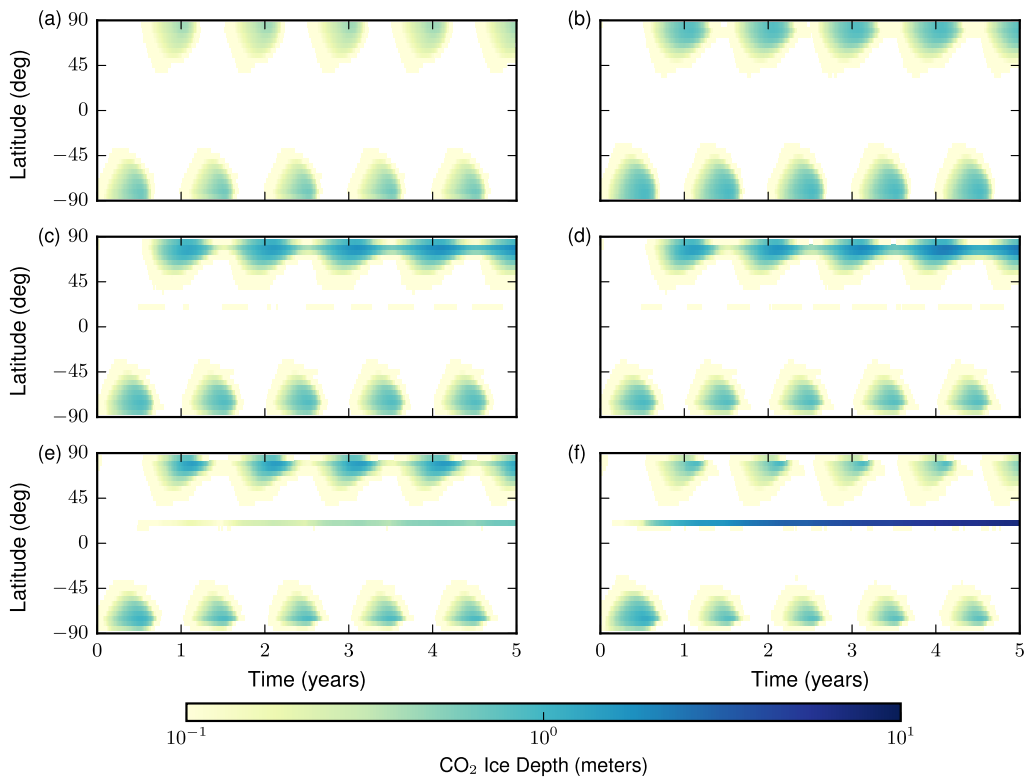**Fig. 5.** Same as Fig. 3 but for 25° obliquity.

Fig. 6. Same as Fig. 3 but for 35° obliquity.

Olympus Mons, which is captured in the MarsWRF model by a single horizontal grid point. As seen in Fig. 3(c)–(f), CO_2 ice forms on this high elevation region at higher CO_2 inventory. We do not

include this CO_2 ice deposition on Olympus Mons in the collapse curves in Fig. 2 since the entire atmosphere can not collapse onto the mountain. Basal melting and ice flow would deliver the CO_2

ice on Olympus Mons to lower elevations, where the CO_2 ice is not stable and therefore would sublimate back into the atmosphere leaving only a small fraction of the total CO_2 ice inventory on the summit and flanks of Olympus Mons, which we discuss in detail below.

As the obliquity of the simulations is increased, a few features of the CO_2 ice deposition change. First, a seasonal rather than perennial deposition of CO_2 ice appears at higher obliquities. Due to the increasing obliquity, the latitudinal extent of the polar winter increases, which leads to a larger region of CO_2 ice deposition during the winter season. The seasonal CO_2 ice extends only a small additional distance equatorward in the $\varepsilon = 5°$ simulations but extends much farther equatorward at higher obliquities, as seen in Figs. 4–6. At higher obliquity the higher CO_2 inventory simulations generate seasonal CO_2 ice at the south polar region. Fig. 4 shows seasonal ice in the southern regions, whereas in Fig. 3 there was no south polar CO_2 ice at the same CO_2 inventories. For all inventories in Fig. 4, the energy balance in the north polar region controls the atmospheric collapse, a result that is found in all collapsing atmospheres for obliquities of 5° to 40°.

The 25° obliquity simulations show a significant transition in the CO_2 ice deposition (Fig. 5). The 6 mb and 3000 mb simulations are no longer collapsing. These two simulations have seasonal CO_2 caps at both poles, but no ice remains during the summer months. This is consistent with the collapse curves show in Fig. 2. The transition from a collapsing atmosphere to a non-collapsing atmosphere actually occurs between $\varepsilon = 15°$ and $\varepsilon = 20°$ obliquity, based on the 20° obliquity simulation results, which are not shown here. For the 6 mb case, the location of this transition between collapsing atmosphere and non-collapsing atmosphere is consistent with previous results by Kreslavsky and Head (2005). None of the collapsing simulations, shown in Fig. 5(b)–(e), have perennial CO_2 ice in the southern hemisphere. Instead, the south pole only experiences a seasonal CO_2 ice cap. Again, deposition of CO_2 ice on the north pole controls the collapse of the atmosphere.

The higher obliquities continue the pattern established at 25° obliquity. The thinnest and thickest atmospheres are stable with respect to CO_2 condensation, with only seasonal CO_2 ice caps appearing in the 6 mb and 3000 mb simulations in Figs. 5 and 6. By 35° obliquity the 60 mb atmosphere has also stopped collapsing, as seen in Fig. 6(b). The collapsing atmospheres (300 mb, 600 mb, and 1200 mb) are increasingly dominated by their seasonal cycles. By the 45° obliquity, all of the simulated CO_2 inventories are stable, with only a seasonal CO_2 cycle and no atmospheric collapse occurring.

We can understand the response of CO_2 to the various global-mean surface pressures and obliquities by comparing our results to the conceptual model in Fig. 1. Should the relationship between the condensation curve and the atmospheric heating by advection and greenhouse warming be as predicted by the conceptual model in Fig. 1, the annual mean polar temperatures in our simulations should lie on or below the sublimation curve for collapsing simulations and lie above the sublimation curve for non-collapsing simulations. Therefore, we plotted the annual-mean surface temperature at each longitude along the 77.5°N latitude for each simulation on a surface pressure versus surface temperature space (Fig. 7). We used the fifth year of the simulations for the following obliquities: $0°, 5°, 15°, 25°, 35°,$ and $45°$. The polar temperatures follow the sublimation curve in a manner similar to that shown in Fig. 1. The collapsing simulations lie on the sublimation curve, since the near surface polar temperatures are held fixed during the collapse process. On the other hand, the non-collapsing simulations, i.e., the 6 mb and 3000 mb simulation, follow the advective and greenhouse heating to temperatures higher than the condensation temperature. The 1200 mb simulation, shown as green circles in Fig. 7(d), represents a simulation in transition. Some

longitudes of the 1200 mb simulation no longer have permanent CO_2 ice, and thus these longitudes appear in Fig. 7(d) as green circles that lie above the CO_2 condensation curve. For other longitudes, perennial CO_2 ice still remains at the surface. These longitudes then appear in Fig. 7(d) as green circles lying on top of the condensation curve.

For the $\varepsilon = 35°$ simulations, the 1200 mb simulation begins to 'move' off the condensation curve, as seen in Fig. 7(e). Collapse is still occurring in the 1200 mb simulation, but the surface area that controls the collapse is smaller at this higher obliquity. At each successively higher obliquity, the same process is seen: the non-collapsing simulations have warm polar temperatures that lie above the condensation curve because the higher obliquity delivers a higher annual-mean insolation to the poles. For the collapsing simulations, with each successively higher obliquity the polar area that accumulates CO_2 ice becomes smaller, thus restricting the rate of atmospheric collapse. By $\varepsilon = 45°$, all of the simulations have stopped collapsing, and the polar surface temperatures have almost entirely moved off the condensation curve. In Fig. 7(f) only one or two locations along the 77.5°N latitude ring, in the 300 mb, 600 mb, and 1200 mb simulations, still lie on the condensation curve. Very little polar area is covered in CO_2 ice, and the atmospheric collapse is essentially stifled.

If we look at the lower obliquity simulations, the process is reversed. More of the simulations lie closer or on the condensation curve. The lower the obliquity, the closer to the condensation curve are the surface temperatures in the north polar area. For the zero obliquity simulations, all of the polar surface temperatures lie on the condensation curve (Fig. 7). (Note that since the CO_2 deposits are more latitudinally confined in the lower obliquity simulations, as previously mentioned, the data in Fig. 7(a) are from the 82.5°N latitudinal ring.) It is not clear from this figure if there still exist either extremely low or extremely high surface pressures for which the polar surface temperature is greater than the local condensation temperature. This becomes important at the low pressure range, particularly in regards to the end stages of atmospheric collapse. When the climates simulated in the zero obliquity case reach CO_2 ice fractions approaching 1, i.e., when the majority of the CO_2 in the system is on the surface of Mars, the martian atmosphere will become very thin. We address the end stage of atmospheric collapse in the next section.

At the higher obliquities, the energy balance in the Olympus Mons region is also changing. Starting with the 0° obliquity simulations (Fig. 3), CO_2 ice accumulates on the Olympus Mons slopes for global-mean surface pressures of 300 mb and higher. This continues until $\varepsilon = 25°$, beyond which CO_2 no longer deposits onto Olympus Mons at 300 mb, though it continues to do so for 600 mb, 1200 mb, and 3000 mb (Fig. 5). By $\varepsilon = 35°$, the CO_2 ice stops condensing onto Olympus Mons in the 600 mb simulation (Fig. 6), and only the 1200 mb and 3000 mb simulations still have CO_2 snows on Olympus Mons at $\varepsilon = 45°$. This change as a function of obliquity of the CO_2 ice on Olympus Mons is due to the competition of increasing insolation at the latitude of Olympus Mons and the surface pressure at Olympus Mons. Although the increased surface pressure of the thicker atmospheres leads to a higher condensation temperature of CO_2, for the 300 mb and 600 mb simulations, this increased condensation temperature is eventually overwhelmed by the increased insolation at the Olympus Mons latitude, which is consistent with the results from other GCM studies (Forget et al., 2013). As well, the surface temperature lapse rate is larger, in magnitude, for higher surface pressures, which contributes to the colder temperatures on Olympus Mons (Forget et al., 2013). For the 1200 mb and 3000 mb simulations, the CO_2 condensation temperature at Olympus Mons has become so high that even the higher insolation at $\varepsilon = 45°$ is insufficient to prevent condensation of CO_2.
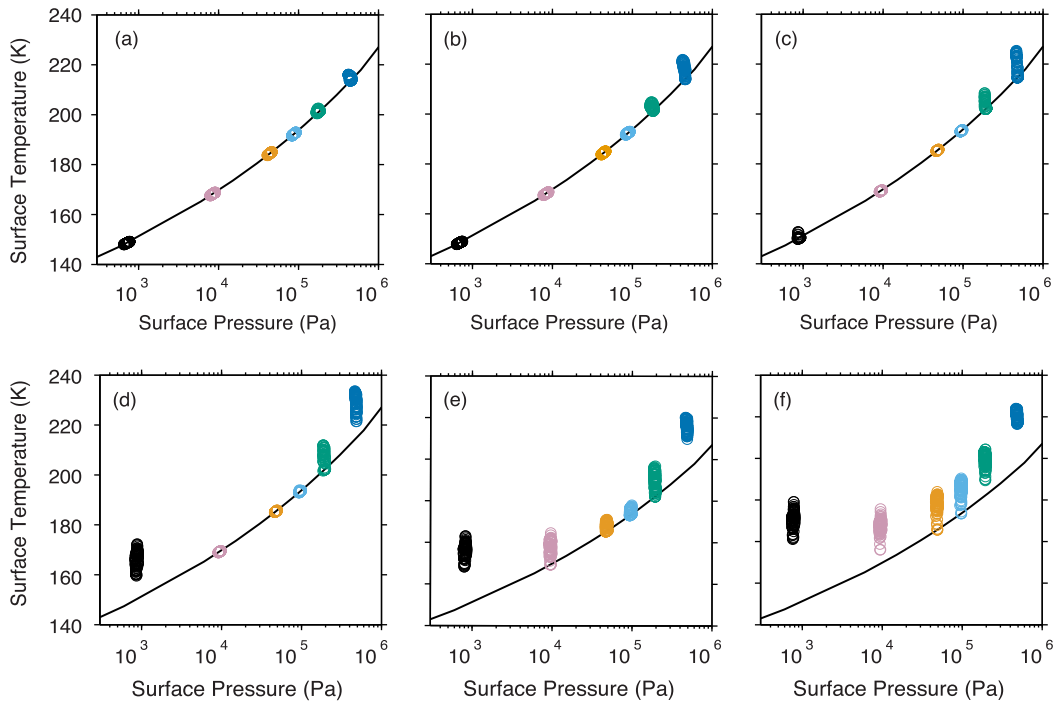
Fig. 7. The annual mean surface temperature versus annual mean surface pressure is plotted for each longitude point along the 77.5°N latitude for the (a) obliquity = 0°, (b) obliquity = 5°, (c) obliquity = 15°, (d) obliquity = 25°, (e) obliquity = 35°, and (f) obliquity = 45° simulations. The black circles are for the 6 mb simulation, the light red circles are for the 60 mb simulation, the orange circles are for the 300 mb simulation, the light blue circles are for the 600 mb simulation, the green circles are for the 1200 mb simulation, and the dark blue circles are for the 3000 mb simulation. The solid black line is the sublimation curve for CO_2. (For interpretation of the references to color in this figure legend, the reader is referred to the web version of this article.)

To understand how the martian climate history is affected by atmospheric collapse and orbital variations, we look at the time required for all of the atmospheric CO_2 to condense onto the surface. The CO_2 ice fraction curves shown in Fig. 2 were fit by linear regression with the goal of calculating a collapse timescale for each simulation. The linear equation of the fit can be written as $f(t) = r_c t + f_0$ where f is the CO_2 ice fraction at time t, f_0 is the 'initial' CO_2 ice fraction, and r_c is the rate of collapse. The simulations begin with an initial ice fraction of zero and spend the first six months of the simulation numerically spinning up. During this period of spin up the CO_2 system is neither linearly growing nor following a seasonal cycle. Therefore we omit this phase from our fit, and the intercept f_0 does not actually capture the initial CO_2 ice fraction. The fitted value of r_c provides us the timescale, τ, since $\tau = 1/r_c$. Fig. 8 shows an example of the fits to the CO_2 ice accumulation curves for a 25° obliquity simulation. The fits to the simulations for the other obliquities are similar: the linear fit captures the long term trend of the CO_2 ice fraction while ignoring the seasonal variations. As well, Fig. 8 shows that the collapsing simulations clearly show a growing accumulation of CO_2 ice when compared to the non-collapsing simulations (i.e., Fig. 8 (a) and (f)). In Fig. 2 this clear difference in CO_2 ice evolution is obscured by the logarithmic scale required to show the global CO_2 ice fractions for each CO_2 inventory in the same plot. Again, this is consistently seen in the simulations for all obliquities.

Table 2 lists the collapse time, in years, for the $\varepsilon = 0°$ to $\varepsilon = 35°$ simulations. There are no collapse times for the 6 mb and 3000 mb simulations for $\varepsilon = 25°$ through $\varepsilon = 45°$ and also the 60 mb, 300 mb, and 1200 mb simulations for $\varepsilon = 45°$, since those simulations are not collapsing. The 600 mb simulation for $\varepsilon = 45°$ is labeled marginal in Table 2, since for this simulation the calculated collapse time is negative, implying non-collapse, but a small amount of perennial ice exists at around 77.5°N latitude. For this

simulation, the majority of longitudes in the polar region have no perennial ice, but a small number of locations have accumulated a few centimeters of CO_2 after five simulation years.

Within each group of similar initial surface pressures (6–3000 mb), the collapse times vary by less than an order of magnitude for the range of obliquities. For example, the 6 mb simulations have a collapse time ranging from 20 years to 100 years for $\varepsilon = 0°$ to $\varepsilon = 15°$. Within each obliquity, the various initial surface pressures have a similar collapse rate, as shown in Tables 2 and 3. A good approximation for the collapse rate, based on the collapse times and collapse rates in Tables 2 and 3, is $\sim10^{15}$ kg yr^{-1}. The collapse rate is controlled by the CO_2 ice surface area, which is similar, to an order of magnitude, between the various simulations. However, our investigation did not address the physical conditions that create the variations in the collapse rates and times. We focused on the threshold for the onset of collapse, thus for our purposes once collapse begins, CO_2 will condense at a rate of $\sim10^{15}$ kg yr^{-1} until the global-mean surface pressure is low enough that the condensation temperatures are below the polar surface temperatures. This transition from collapsing to non-collapsing is determined by the obliquity of Mars, as shown above.

The collapse times are significantly shorter than the 120,000 year period of the obliquity oscillations (Ward, 1974). Indeed, the atmosphere either collapses rapidly or not at all. For the 6 mb and 3000 mb CO_2 inventories, the martian atmosphere would completely collapse when the obliquity oscillations dip below $\varepsilon = 20°$. Such conditions occur in many of Laskar et al.'s (2004) obliquity calculations. Interestingly, for the middle range of global-mean surface pressures, i.e., from ~60 mb to ~1200 mb, the martian atmosphere would completely collapse up to $\varepsilon = 40°$, which includes a much larger portion of the likely obliquity values for Mars (Laskar et al., 2004). Laskar et al. (2004) calculated that over 4 billion years, the mean expected obliquity
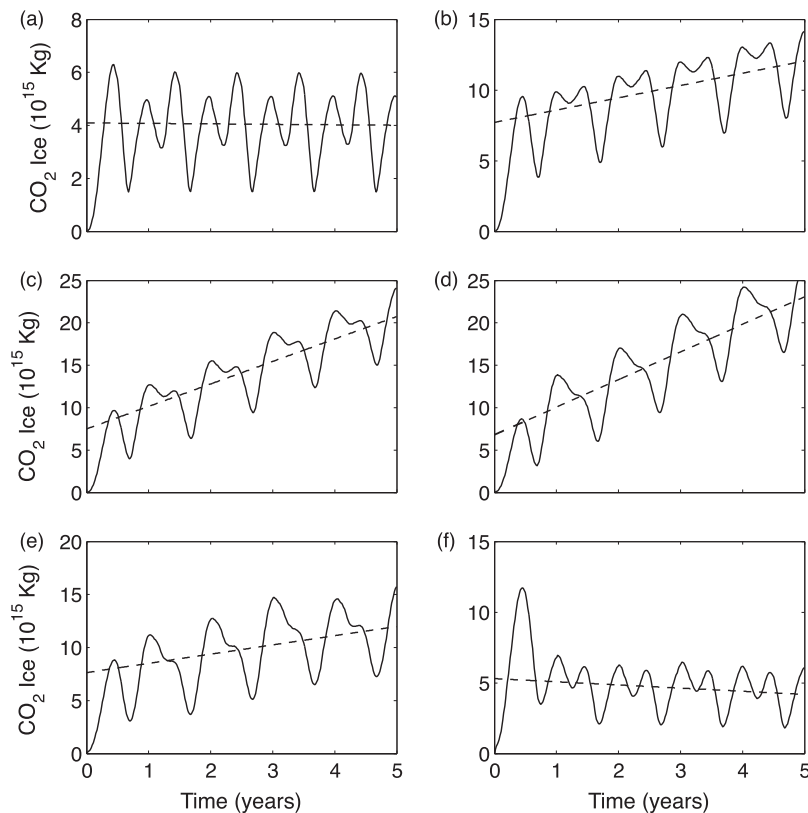
Fig. 8. Linear regression fits to the CO_2 accumulation for the 0° obliquity simulations at the current solar luminosity. Fits are shown for the (a) 6 mb, (b) 60 mb, (c) 300 mb, (d) 600 mb, (e) 1200 mb, and (f) 3000 mb simulations. The solid black line is the accumulated global CO_2 ice and the dotted line is the linear regression.

Table 2
Atmospheric collapse times, in years. NC = not collapsing.

$\bar{P}_s$	Obliquity					
	0°	5°	15°	25°	35°	45°
6	20	20	100	NC	NC	NC
60	90	70	120	300	NC	NC
300	700	400	500	500	2200	NC
600	1900	1200	900	900	2100	Marginal
1200	6500	4100	4300	6500	NC	NC
3000	14,500	12,300	36,300	NC	NC	NC

of Mars is $\bar{\varepsilon} = 37.62°$ with a standard deviation of $\sigma_\varepsilon = 13.814°$. Within this range, the most probable obliquity for Mars over 4 billion years is $\varepsilon = 41.80°$ (Laskar et al., 2004). Therefore, for the current solar luminosity, a pure CO_2 atmosphere within a mid-range of CO_2 inventories, i.e., ~100 mb to ~1000 mb, would have undergone collapse for a significant fraction of the probable range of obliquities.

6. The end of collapse: a vapor pressure balanced climate

As we have shown, the various CO_2 inventories undergo atmospheric collapse for a large range of obliquities. The collapse time is shorter than the period of the obliquity cycle. Thus, for the current luminosity, the martian atmosphere would completely collapse during a period of low obliquity. What does complete atmospheric collapse entail? As discussed in the introduction, the conceptual model shown in Fig. 1 has a lower bound to the region of collapse. At point A in Fig. 1, the climate is at a stable equilibrium point. Therefore, the surface pressure in a collapsing atmosphere will slowly decrease and the atmosphere would move left on the sublimation curve in Fig. 1 until reaching point A. Once sufficient CO_2 has condensed onto the polar surfaces that the surface pressure corresponds to point A in Fig. 1, the atmosphere would be in a stable equilibrium with the surface CO_2 ice. Atmospheric collapse would thus cease. When atmospheric collapse ends, the martian atmosphere is in vapor pressure balance with large CO_2 ice sheets in the polar regions.

We cannot use the collapse simulations that we presented above to investigate the end of collapse because, except for the

Table 3
Atmospheric collapse rates, in kg/year. NC = not collapsing.

$\bar{P}_s$	Obliquity					
	0°	5°	15°	25°	35°	45°
6	1.4×10^{15}	1.4×10^{15}	0.3×10^{15}	NC	NC	NC
60	3.1×10^{15}	4×10^{15}	2.3×10^{15}	0.9×10^{15}	NC	NC
300	2×10^{15}	3.5×10^{15}	2.8×10^{15}	2.8×10^{15}	0.6×10^{15}	NC
600	1.5×10^{15}	2.3×10^{15}	3.1×10^{15}	3×10^{15}	1.3×10^{15}	Marginal
1200	0.9×10^{15}	1.4×10^{15}	1.3×10^{15}	0.9×10^{15}	NC	NC
3000	1×10^{15}	1.1×10^{15}	0.4×10^{15}	NC	NC	NC

Table 4
The polar CO_2 ice mass and depth used to test the end of atmospheric collapse.

Inventory name	Inventory mass (kg)	Ice column mass (kg/m²)	Ice depth (m)
6 mb	0.028×10^{18}	1740	~1.1
60 mb	0.28×10^{18}	17,400	~11
300 mb	1.4×10^{18}	87,000	~54
600 mb	2.8×10^{18}	174,000	~110
1200 mb	5.6×10^{18}	348,000	~220
3000 mb	14.0×10^{18}	870,000	~550

shortest collapse times in Table 2, the collapse times are too long to simulate with the MarsWRF GCM. Instead, we have run simulations that start with almost all of the CO_2 inventory as surface ice in the polar regions. These simulations, which we refer to as 'inflation' simulations, are the reverse of our collapse simulations. Each inflation simulation was initialized with a global-mean surface pressure of 1 mb and the rest of the CO_2 inventory as ice on the polar surface. Thus, each inflation simulation has ~4.7×10^{15} kg of CO_2 in the atmosphere. The remaining CO_2 is surface ice uniformly distributed over the latitudes 67.5°N to 90°N and latitudes 67.5°S to 90°S. The equivalent CO_2 ice depth is shown in Table 4.

Fig. 9 shows an example of the inflation simulation results. This particular simulation started with a 54 m thick ice cap on both poles (300 mb inventory shown in Table 4) and uses an obliquity of 25°. Fig. 9 shows the global-mean surface pressure as a function of time. At the beginning of the simulation, CO_2 ice sublimes thereby increasing the global-mean surface pressure. By the end of the first five years of the simulation the climate achieves an equilibrium global-mean surface pressure of ~25 mb, while maintaining the distinctive seasonal cycle of the martian surface pressure. This simulation still has a large CO_2 inventory (see Table 4) but the bulk of the CO_2 remains as ice on the polar surface. This is essentially the CO_2 vapor-ice balance identified by Leighton and Murray (1966). Under these conditions, the atmosphere is in vapor pressure balance with the surface CO_2 ice and remains so until the net insolation is sufficient to completely sublime the surface CO_2 ice, i.e., surface temperature increases and 'drives' the climate to the right of point B in Fig. 1.

The same phenomenon is seen in almost all collapsing simulations for $\varepsilon = 25°$. The 60 mb, 300 mb, 600 mb, and 1200 mb inventory inflation simulations all evolve to have a global-mean surface pressure of 25 mb with CO_2 ice sheets covering the poles. The amount of atmospheric CO_2 of a stable yet fully collapsed atmosphere is a function of obliquity and solar luminosity, with the global-mean surface pressure of the stable climate increasing with increasing obliquity. This can be seen in Fig. 7(e): for $\varepsilon = 35°$ the
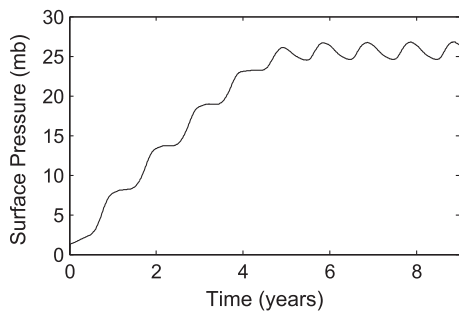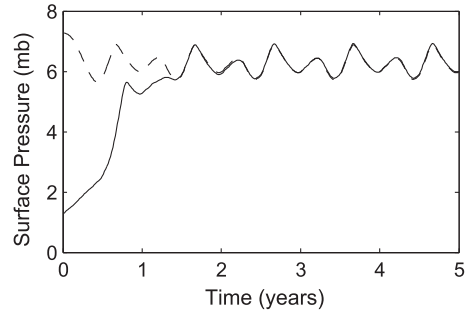

Fig. 10. The global-mean surface pressure as a function of time for the $\varepsilon = 25°$ for a 6 mb CO_2 inventory. The solid black line is for the inflation simulation, where the simulation starts with most of the CO_2 inventory as ice at the poles except for a 1 mb atmosphere; the dashed black line is for the collapse simulation, where the simulation starts with all of the CO_2 inventory as gas in the atmosphere.

stable point (i.e., point A in Fig. 1) shifts to a global-mean surface pressure between 60 mb and 300 mb.

To ensure that the stable point at the end of atmospheric collapse does not vary due to initial conditions (i.e., collapse versus inflation), we ran an inflation simulation for a non-collapsing CO_2 inventory, in this case the 6 mb inventory at $\varepsilon = 25°$. Fig. 10 shows the evolution of the global-mean surface pressure for two simulations: a simulation where all of the CO_2 begins in the atmosphere (i.e., the 'collapse' simulation) and a simulation where almost all of the CO_2 begins as ice at the poles (i.e., the 'inflation' simulation). Both the collapse and the inflation simulation achieve the same steady state within two Mars years. The steady state is a climate with a global-mean surface pressure of ~6 mb and a seasonal CO_2 cycle. Fig. 10 demonstrates that the steady state climate is not dependent on the initial condition of the CO_2. For a given CO_2 inventory, collapsing and inflating atmospheres evolve to the same final state. Thus, we feel confident that results like that shown in Fig. 9 represent the end state of atmospheric collapse.

7. Limits on the height of CO₂ ice caps

Ultimately there is a limit to the amount of carbon dioxide ice that can be deposited at a particular point on the martian surface. The height of an ice cap is limited by at least two processes: first, the mechanical failure of ice under its own weight, which leads to horizontal flow of the ice, and second, the basal melting due to geothermal heating and overburden pressure, which can lead to horizontal transport of CO_2 liquid. For the current martian atmosphere, a polar cap of carbon dioxide ice can maintain a thickness of around 1800 m for around 10^7 years before the ice mechanically fails under its own weight (Nye et al., 2000). Additionally, as the CO_2 ice piles up, the base of the ice cap heats up until the ice is converted into liquid, a process called basal melting (Mellon, 1996). Once basal melting begins, liquid CO_2 can flow into the subsurface thus limiting the accumulation of CO_2 ice to ~1200 m in the current martian atmosphere (Mellon, 1996).

To determine order of magnitude constraints on CO_2 ice deposition, we extended the Mellon (1996) calculations on basal melting of CO_2 ice sheets to the range of atmospheric pressures that we have investigated. The thermal limits on polar cap height involve a balance between the increasing pressure and the increasing temperature at depth within the cap. Similar to Mellon (1996), we calculated the pressure within the cap using the following relation:

$$P(z) = P_s + \rho g z \tag{1}$$

where P_s is the surface pressure at the top of the cap, ρ is the density of the CO_2 ice, g is the gravity on Mars, and z is the depth in the

Fig. 9. The global-mean surface pressure as a function of time for the $\varepsilon = 25°$ for a 300 mb CO_2 inventory, where the simulation starts with most of the CO_2 inventory as ice at the poles except for a 1 mb atmosphere.

ice. The equilibrium temperature at depth within the polar cap is calculated using:

$$T(z) = T_s + \frac{H}{k}z \qquad (2)$$

where T_s is the surface temperature at the top of the ice cap, H is the geothermal heat flux from below the ice cap, and k is the effective thermal conductivity of the carbon dioxide ice (Mellon, 1996). Like Mellon (1996), we use a CO_2 effective thermal conductivity of 0.5 W m^{-1} K^{-1} and a geothermal heat flux of 0.03 W m^{-2}. For this calculation, the CO_2 ice density is 1600 kg m^{-3} (Kieffer, 2007). The ice cap surface temperature is the sublimation temperature for the given CO_2 inventory. For a 6 mb atmosphere the condensation temperature is $\sim$148 K; for a 3000 mb atmosphere the condensation temperature is $\sim$208 K. Fig. 11 shows the polar cap thickness temperature–pressure profiles for the atmospheric thicknesses of our simulations.

The results of this simple model provide some constraints on our simulation results. As seen in Fig. 11, a cap thickness of 100s of meters is achievable for all CO_2 inventories. Thicker CO_2 ice caps are possible for thin atmospheres, but for thick atmospheres, particularly the 3000 mb simulation, cap thickness much greater than 100 m quickly cross the ice-liquid phase boundary and thus CO_2 ice will begin melting at the base of the ice deposit. Unable to sustain further CO_2 ice, the CO_2 liquid may be squeezed out of the base. Additionally, for CO_2 ice lying on slopes, the basal melting may facilitate flow of the CO_2 ice sheets. If the CO_2 ice does start flowing, the flow itself could double the heating at the base of the CO_2 ice sheet and accelerate the basal melting (Mellon, 1996). At complete collapse, the thinnest atmosphere would have ice sheet thicknesses on the order of meters to tens of meters at each polar cap. For the 600 mb simulation, the CO_2 ice sheets would be on the order of 100s of meters thick, which puts those deposits near the height associated with basal melting. The thickest atmospheres would not be able to completely collapse before basal melting occurred. Since these thick atmosphere simulations take the longest time to completely collapse, it is possible that these climate systems possess further CO_2 stability regimes where CO_2 basal melting limits further collapse and the CO_2 gas, liquid, and ice inventories achieve a sustainable balance. Determining such possible regimes is beyond the scope of this investigation and is left for future work.

Our simple extension of the work of Mellon (1996) omitted many complexities, including the different densities for different types of CO_2 ice, like pure CO_2 ice or CO_2 firn, the range of possible geothermal heat fluxes, effect of local slopes, and the range of possible thermal conductivity for both pure ice and ice mixtures. Our simulations using MarsWRF explored the atmospheric physics involved in the collapse of the martian atmosphere, but further work on the physics of CO_2 ice will be required to understand the final distribution of CO_2 ice.

8. Condensation versus atmospheric heating

The martian polar climate is subject to four feedbacks that affect the energy balance in the atmosphere (McKay et al., 1991; Nakamura and Tajika, 2002). The ice-albedo feedback is a positive feedback where the deposition of ice decreases the surface temperature, leading to more ice deposition. Another positive feedback is the greenhouse effect, where the generation of additional atmospheric CO_2, usually by subliming CO_2 ice, warms the atmosphere, leading to the generation of more atmospheric CO_2. A third positive feedback in the polar regions is the heat transport feedback. An increase in global atmospheric mass leads to an increase in the strength of the equator-to-pole atmospheric heat transport, which then sublimes surface CO_2 ice, increasing the global atmospheric mass. The fourth feedback, the condensation temperature feedback, is a negative feedback: as atmospheric pressure increases, the condensation temperature of CO_2 increases, leading to increased CO_2 condensation and a reduction of the atmospheric pressure. The heat transport feedback and the greenhouse feedback work to increase the atmospheric pressure and decrease the CO_2 ice inventory, while the ice-albedo feedback and the condensation temperature feedback both promote the deposition of CO_2 ice.

In the energy balance of the polar regions, these feedbacks are competing to determine the surface temperature and climate state. Whether an energy balance model is used or a general circulation model, correctly capturing this feedback competition is important for correctly determining the polar surface temperature and climate state. In previous work, the heat transport feedback was calculated using a diffusive term based on radiative–convective calculations (Gierasch and Toon, 1973; Haberle et al., 1994; Nakamura and Tajika, 2002) while using gray atmosphere approximations for the radiative transfer (Gierasch and Toon, 1973; McKay et al., 1991; Haberle et al., 1994; Manning et al., 2006; Nakamura and Tajika, 2002). We have leveraged the numerical solution of the primitive equations for atmospheric dynamics in the GCM to more accurately simulate the atmospheric heating in the polar regions. This has allowed us to more closely investigate the competition between the atmospheric heating feedbacks and the atmospheric cooling feedbacks.

The competing relationship between the condensation temperature feedback and the atmospheric heating feedback explains why the mid-range global-mean surface pressure simulations continue to collapse at $\varepsilon = 25°$, while the thinnest and thickest atmospheres have ceased collapsing. The two non-linear effects swap dominance more than once over the range of atmospheric pressures we explored. The range of surface pressures that experience collapse is larger in our simulations than in the work of McKay et al. (1991) and Haberle et al. (1994). Whereas McKay et al. (1991) and Haberle et al. (1994) found the range of global-mean surface pressures that lead to atmospheric collapse to be $\sim$5 mb to $\sim$50 mb, our simulations have atmospheric collapse occurring between $\sim$25 mb and $\sim$1200 mb. Greenhouse and/or advective heating are actually less efficient in the GCM simulations than in the energy balance models for the middle range of global-mean surface pressures. Some of this difference between our results and previous results is due to topography, which our models capture but is often left out of the energy balance models. In
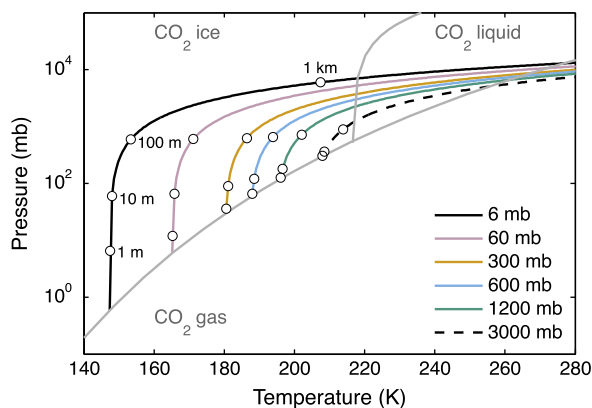

Fig. 11. Temperature–pressure profile of a polar CO_2 ice cap compared to the CO_2 phase diagram. The gray lines are the phase boundaries for CO_2 in a single-component system. The regions of CO_2 gas, CO_2 liquid, and CO_2 ice are identified. The profiles correspond to the six different CO_2 inventories of this investigation. Each profile is marked by four depth levels: 1 m, 10 m, 100 m, and 1 km.

particular, the permanent CO_2 ice caps are primarily in the northern hemisphere due to the higher surface pressure in the northern lowlands, which leads to higher condensation temperatures, requiring greater heat transport to offset CO_2 condensation. When the southern hemisphere annual-mean surface temperatures for 77.5°S latitude are plotted similarly to Fig. 7, all of the southern hemisphere points lie above the condensation curves, at lower surface pressures than for the northern hemisphere. As we shall see in the following section, the advective heating is weaker than expected due to the unique topography of Mars, which explains the wider range of surface pressures for which collapse occurs.

The different obliquities shift the polar surface temperatures with respect to the condensation curve, which is shown conceptually in Fig. 12. Higher obliquity delivers more insolation to the polar region for all CO_2 inventories and thus shifts the polar temperatures higher. Similarly, lower obliquity shifts the temperatures lower. For most of the obliquities we simulated, the polar surface temperature curve intersects with the condensation temperature curve as previously described. When the obliquity increases sufficiently, to $\varepsilon = 45°$ in our simulations, the polar temperature curve lies completely above the condensation curve, and atmospheres will not collapse at any CO_2 inventory. This transition to non-collapsing atmospheres occurs because there is enough insolation in the polar region to allow the atmospheric heating feedbacks to overwhelm the condensation temperature feedback.

9. The meridional transport of energy and atmospheric collapse

One of the goals of this investigation was to understand how the threshold for collapse changed when using a GCM in which the meridional transport of energy is resolved. As discussed, the range of atmospheric collapse, as a function of the total CO_2 inventory, is wider in the GCM results than previously thought. To understand how the meridional transport of energy affects the conditions for atmospheric collapse, we looked at a Reynolds decomposition of the annual mean meridional transport of dry static energy.

The dry static energy is defined as $E = gz + c_pT$ where g is gravity, z is height, c_p is the specific heat capacity, and T is the air temperature. The dry static energy consists of the atmospheric potential energy, gz, and the atmospheric enthalpy, c_pT; it is the relevant energy for transport considerations (Peixoto and Oort, 1992). The meridional transport of dry static energy is represented by vE where v is the meridional wind velocity. We then used Reynolds decomposition to identify the mean circulation, stationary eddy, and transient eddy terms of the meridional transport (Reynolds, 1895; Peixoto and Oort, 1992).

Generally, a diagnostic field can be decomposed into a mean field and a perturbation field (Reynolds, 1895). A quantity is related to the temporal mean and temporal perturbation by $(\cdot) = \overline{(\cdot)} + (\cdot)'$, where $\overline{(\cdot)}$ is the temporal mean of the quantity $(\cdot)$ and $(\cdot)'$ is the temporal perturbation.[3] A quantity is related to the zonal-mean and zonal perturbation by $(\cdot) = [\cdot] + (\cdot)^*$, where $[\cdot]$ is the zonal-mean of the quantity $(\cdot)$ and $(\cdot)^*$ is the zonal perturbation. The decomposition of the zonal and temporal mean of the total transport, $[\overline{vE}]$, is

$$[\overline{vE}] = [\overline{v}]\,[\overline{E}] + [\overline{v^*\overline{E}^*}] + [\overline{v'E'}] \tag{3}$$

[3] In order to properly account for the divergent mass fields that occur due to the large topographical changes on Mars and the use of σ-coordinates in the MarsWRF model, we define the time mean as $\overline{(\cdot)}^w = \overline{(P_s\cdot)}/\overline{P_s}$ where P_s is the surface pressure; this formulation is the "mass-weighted" mean (Andrews et al., 1987). Similarly, we define the mass-weighted zonal-mean as $[\cdot]^W = [P_s\cdot]/[P_s]$. For simplicity, we omit the 'w' superscript, although all of the means in this paper are mass-weighted means.
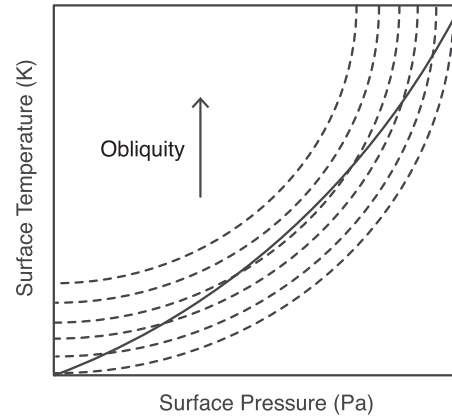

Fig. 12. The interaction between obliquity, polar surface temperature due to atmospheric heating, and the condensation curve. The solid black line represents a condensation curve for CO_2. The dashed black lines represent polar surface temperature as a function of surface pressure. Each dashed line represents the polar surface temperature at a given obliquity. The obliquity increases towards the top of the figure.

where $[\overline{v}]\,[\overline{E}]$ is the mean circulation term, $[\overline{v^*\overline{E}^*}]$ is the stationary term, and $[\overline{v'E'}]$ is the transient term (Peixoto and Oort, 1992). With this decomposition, we can determine whether a particular atmospheric phenomenon is controlled by larger-scale circulation as shown by the mean circulation term, $[\overline{v}]\,[\overline{E}]$, or by the stationary and/or transient eddy terms, $[\overline{v^*\overline{E}^*}]$ and $[\overline{v'E'}]$. Each of the terms in Eq. (3) is vertically integrated and therefore a one-dimensional term that is a function of latitude; for simplicity, we do not explicitly denote the vertical integration in the decompositions discussed below.

We applied the Reynolds decomposition to the annual mean dry static energy, as shown in Fig. 13. The annual mean meridional transport in the 6 mb simulation, shown in Fig. 13(a), is dominated by the mean circulation, which is moving energy northward across the equator. Stationary and transient eddies in the northern hemisphere play a smaller role in the northward transport of energy. In the southern hemisphere, however, the stationary and transient eddy transports oppose each other. The combination of the mean circulation and stationary eddies lead to a net southward transport of energy in the southern hemisphere, but this southward transport of energy is much smaller, annually, than the northward transport in the northern hemisphere.

The simulations with larger CO_2 inventories, however, have a very different distribution of meridional energy fluxes. At around 15–20°N, the larger CO_2 inventory simulations exhibit a sharp spike in the meridional transport. This spike is dominated by northward transport of energy from adjacent latitudes to the south (see Fig. 13(b)–(f)). For the largest inventories, there is a smaller southward transport of energy that is also delivering energy into the 15–20°N region. Essentially, the mean circulation transports energy into a narrow latitude range in the northern tropics.

What is driving this mean circulation transport? The dominant features at these latitudes are Olympus Mons and the Tharsis Montes, and thus these features are the likely candidates for driving this peculiar feature in the meridional transport. The transient and stationary eddy transports show no corresponding transport of energy into this region. Since the spike in the meridional transport is restricted to the mean circulation, the source of this spike must be sustained throughout the martian year. Fig. 5 shows that CO_2 condenses continuously onto the Olympus Mons and Tharsis Montes region for the simulations with greater CO_2 inventory. Thus, to investigate this spike in meridional transport, we further decomposed the mean circulation into an overturning circulation and a condensation flow.
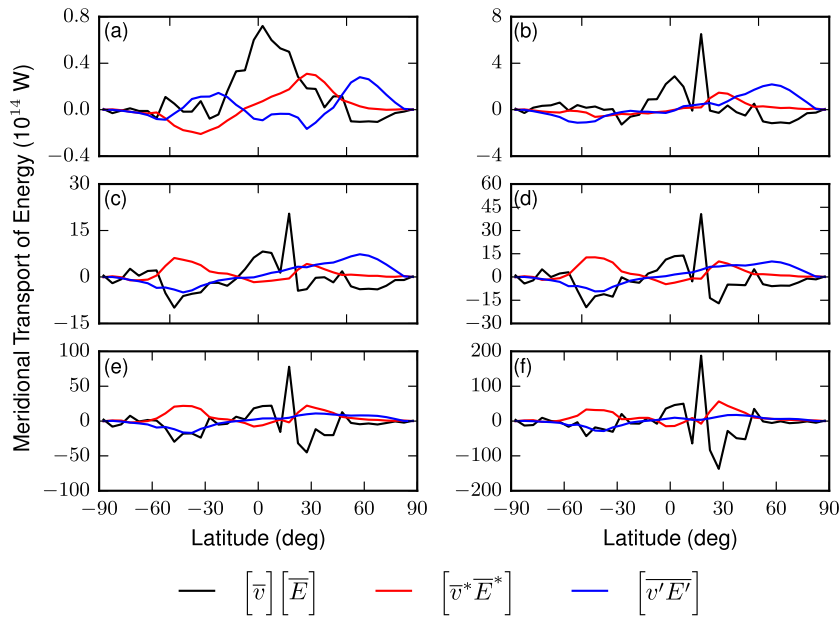
Fig. 13. The annual-mean meridional transport of dry static energy as a function of latitude for different mean surface pressure. The panels are for mean surface pressures of (a) 6 mb, (b) 60 mb, (c) 300 mb, (d) 600 mb, (e) 1200 mb, and (f) 3000 mb. The solid black line is the mean circulation, $[\overline{v}]\,[\overline{E}]$, the red line is the transient eddies, $[\overline{v'E'}]$, and the blue line is the stationary eddies, $[\overline{v}^*\overline{E}^*]$. (For interpretation of the references to color in this figure legend, the reader is referred to the web version of this article.)

When atmospheric CO_2 condenses on the surface, the total mass of atmospheric CO_2 changes, which also changes the magnitude and distribution of the atmospheric surface pressure (Tillman et al., 1993; Hess et al., 1979). The atmosphere adjusts to these changes by shifting the CO_2 mass from adjacent columns; this adjustment of the column mass due to condensation of an atmospheric constituent is known as condensation flow (Leovy and Mintz, 1969; Pollack et al., 1981, 1990; Peixoto and Oort, 1992). The CO_2 condensation flow is the flow that remains when the meridional velocity is vertically mass-averaged (Pollack et al., 1990). The condensation flow is calculated by taking the mass-weighted vertical average of velocity at each latitude:

$$\langle[\overline{v}_c]\rangle = \int_1^0 \left[\overline{(P_s - P_t)v}\right]\mathrm{d}\sigma/\left[\overline{P_s - P_t}\right] \qquad (4)$$

where v is the total meridional velocity at each vertical level, P_t is a constant pressure at the top of the model domain, P_s is the surface pressure, $\sigma = (P - P_t)/(P_s - P_t)$ is the vertical coordinate, $(P_s - P_t)$ is the column pressure, and $\langle\cdot\rangle$ indicates a vertical mean (Pollack et al., 1981).

With this condensation flow velocity, we calculated the vertically integrated meridional transport of energy due to the condensation flow, $\langle[\overline{v}_c]\rangle[\overline{E}]$. With the standard mean circulation term, $[\overline{v}]\,[\overline{E}]$, and the condensation flow term applied at each vertical level, we then calculated the meridional transport of energy due to the "overturning circulation", ξ, by:

$$\xi = [\overline{v}]\,[\overline{E}] - \langle[\overline{v}_c]\rangle[\overline{E}]. \qquad (5)$$

This method for separating the mean portion of the meridional transport is similar to methods previously used by Leovy and Mintz (1969), Pollack et al. (1981), Pollack et al. (1990), Haberle et al. (1993). Fig. 14 shows the mean meridional wind decomposed into a condensation flow and an overturning flow for the six different CO_2 inventories; the mean circulation in Fig. 14 is the same as shown in Fig. 13. The overturning circulation transport represents the energy transport due to the traditional large-scale circulation, e.g., the thermally direct Hadley circulation or the thermally indirect Ferrell circulation. In all simulations, the condensation flow

creates the high variability in energy transport seen in the total mean circulation and is responsible for a large fraction of the sharp spike of meridional energy transport into the 15–20°N region. The overturning circulation also contributes to this spike in the meridional transport of energy. After five Mars years, the condensation flow has affected the overturning circulation and the two processes become coupled. Even with this coupled response, the meridional transport due to condensation flow in the Tharsis region matches or exceeds the meridional transport due to the overturning circulation in the large CO_2 inventories, as seen in Fig. 14(e) and (f).

For the 6 mb simulation (Fig. 14(a)), the condensation flow does not show any consistent structure. This is a non-collapsing simulation (see Fig. 5(a)) so no systematic condensation flow is expected. The seasonal averages for the northern summer and winter (not shown), however, do show a condensation flow to the winter pole as CO_2 condenses on to the winter polar surface. These seasonal condensation flows have the same structure and magnitude as those seen in previous simulations of condensation flows on Mars (Leovy and Mintz, 1969; Pollack et al., 1981, 1990; Haberle et al., 1993). For the larger CO_2 inventories a sharp spike in the condensation flow appears at the same latitude as the spike in meridional energy transport seen in Fig. 13.

Despite the strength of the condensation flow onto Olympus Mons, the atmospheric collapse is still controlled by the condensation onto the polar region over the long term. Although we can not directly simulate this assertion, we can use a conceptual view of the condensation flow process to illustrate the important difference between the polar condensation flow and the Olympus Mons condensation flow. In the polar region, the collapse process has a single direction: when there is insufficient heating of the near-surface polar atmosphere CO_2 condenses onto the surface. The only way to reverse this process is to increase the planet's obliquity, thereby increasing the annual-mean insolation at the pole (see Section 6). On Olympus Mons, however, the slopes of this mountain generate a "condensation flow circulation". Once sufficient CO_2 ice accumulates on the slopes of Olympus Mons, the CO_2 ice moves downslope due to the combination of basal melting and local slope (this process is not included in the GCM simulations). As shown previously, the larger CO_2 inventories will reach
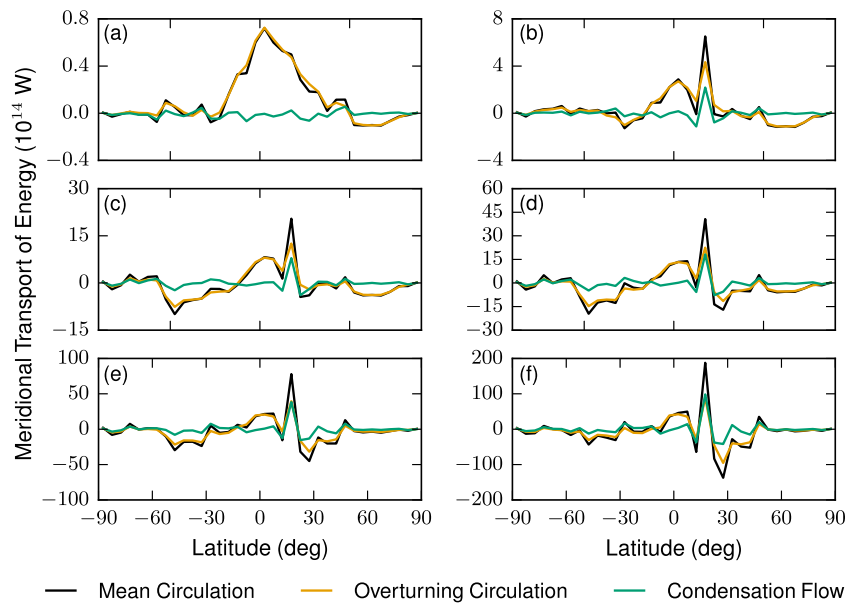
Fig. 14. The annual mean meridional transport of dry static energy as a function of mean surface pressure. The mean transport is decomposed into the transport due to overturning cells and the transport due to condensation flow. The plots include the following initial surface pressures: (a) 6 mb, (b) 60 mb, (c) 300 mb, (d) 600 mb, (e) 1200 mb, and (f) 3000 mb. The solid black line is the total mean circulation, $[\overline{v}]\,[\overline{E}]$, the orange line is the overturning circulation, ξ, and the green line is the condensation flow, $[\overline{v}_c]\,[\overline{E}]$. (For interpretation of the references to color in this figure legend, the reader is referred to the web version of this article.)

sufficient thickness for basal melting. The combination of the rapid deposition of CO_2 ice onto Olympus Mons (see Figs. 3–6) and the shallow but extensive slope of Olympus Mons (Aharonson et al., 1998) contributes to the eventual movement of the CO_2 ice and the limit on maximum accumulation of CO_2 ice in this region. At lower elevations, the CO_2 ice will no longer be stable and thus sublimate, returning CO_2 to the atmosphere. This essentially creates a "condensation flow circulation", but on a time scale longer than we could run in our GCM simulations. Thus, there is an upper limit on the amount of CO_2 ice that will accumulate on the surface of Olympus Mons and the adjacent mountains. For atmospheric collapse to occur, the steady accumulation of CO_2 ice must occur in the polar regions. (This is why the accumulation of CO_2 ice in the Olympus Mons region was omitted from the CO_2 ice growth curves shown in Fig. 2 and discussed in Section 5.) A large fraction of the meridional energy transport is being diverted to the northern mid-tropics by the condensation flow on to the Olympus Mons and the Tharsis Montes (Fig. 14).

However, the condensation of CO_2 onto Olympus Mons still plays an important role in the onset of atmospheric collapse. Even with a condensation flow circulation over the slopes of Olympus Mons, the energy transport associated with condensation flow near Olympus Mons dwarfs the energy transport of the condensation flow near the polar regions. Thus, the condensation at Olympus Mons is monopolizing energy that would likely otherwise be transported into the north polar region. This is one reason why our GCM simulations had a larger range of collapse than predicted by energy balance models.[4] Instead of an increase in the poleward advection of energy from a stronger circulation due to increasing atmospheric CO_2 inventory as predicted by Haberle et al. (1994) and others, the condensation of CO_2 ice onto Olympus Mons diminishes the poleward energy transport into polar regions.[5]

---

[4] Stationary eddy energy transport, often overlooked in EBMs, also contributes.

[5] It is interesting to note that Fig. 14(f) shows that even when collapse no longer occurs, the condensation flow circulation on the slopes of Olympus Mons still dominates the meridional transport of energy for large CO_2 inventories.

10. Conclusions

We have shown that for obliquities less than 20°, perennial CO_2 ice will form for all inventories, up to 3000 mb. Even thick atmospheres are insufficient to stave off atmospheric collapse. The distribution of the perennial ice is dependent on both the condensation temperature of CO_2 at the surface and the combination of the greenhouse effect of the atmosphere and the meridional transport of energy in the atmosphere. In fact, these processes compete to determine where and at what elevation the CO_2 ice accumulates. Regardless of the distribution of the CO_2 ice, the timescale for deposition is much longer than that produced by a 1-D model.

For the lower obliquities, the tendency for the atmosphere to collapse is not a function of the atmospheric mass for the range of masses that we considered. At all CO_2 inventories, at least one polar cap is collapsing. What is controlled by the atmospheric mass in the lower obliquity simulations is the condensation of CO_2 in the southern hemisphere, where elevations are higher. At the low obliquities, the thicker atmospheres provide enough heating to prevent perennial ice from forming in the southern hemisphere. For the higher obliquity simulations, however, the collapse tendency varies with atmospheric mass. The lowest mass atmospheres and the highest mass atmospheres do not collapse. The mid-range atmospheric masses continue to experience collapse and deposition of polar CO_2 ice up to an obliquity of 45°.

The obliquity has a much stronger control on the tendency to collapse than the atmospheric mass. The interaction of the polar surface temperature with the condensation temperature is strongly controlled by the distribution of insolation, which in turn is controlled by the obliquity of the planet. For low obliquities, the polar temperature is less than the condensation temperature for all CO_2 inventories simulated. The increasing obliquity increases the polar temperature. The low and high CO_2 inventory simulations are the first to warm enough to have polar surface temperatures greater than the condensation temperature. Higher obliquities continue to control the relationship between the polar surface

temperature and the condensation temperature, and therefore the tendency of the atmosphere to collapse.

This work does not treat some important processes that could affect our results. The orbital eccentricity affects the annual cycle of insolation, and therefore could influence the onset of collapse as well as the overprinting of the seasonal cycle of CO_2. Atmospheric dust activity and variations in ice albedo may have changed the location of the stability points of the martian climate (Kahre et al., 2013). By providing an internal heating source to the atmosphere, atmospheric dust may also have narrowed the range of pressures and obliquities under which the atmosphere collapses (Davies, 1979; Forget et al., 2013; Kahre et al., 2013). At the same time, the mixing of dust and rock into the carbon dioxide ice may have lowered the ice albedo thereby limiting the onset and extent of atmospheric collapse. Similarly, we did not explore how the albedo of CO_2 ice may affect the atmospheric collapse problem, though this has been investigated by Kahre et al. (2013) for the early Mars environment. Finally, the ancient martian atmosphere would have received less insolation due to a fainter Sun, which would change the threshold for atmospheric collapse (Gough, 1981; Gilliland, 1989). Our understanding of Mars' unique mechanism for meridional energy transport derived from this investigation will provide a solid starting point to explore this unaddressed process.

The results of our simulations match the polar surface temperature and surface pressure relationship developed by Gierasch and Toon (1973), McKay et al. (1991), and Haberle et al. (1994). We find, however, that the range of atmospheric thicknesses that undergo atmospheric collapse is larger than seen in the previous energy balance models. The range of global-mean surface pressures at which collapse occurs at an obliquity of $25°$ spans two orders of magnitude in our GCM simulations, whereas previous EBM simulations found a range that spans only one order of magnitude (Gierasch and Toon, 1973; McKay et al., 1991; Haberle et al., 1994). We originally expected that the larger CO_2 inventories would have avoided atmospheric collapse at much lower obliquities due to the larger thermal mass in the thicker atmospheres and the presumed higher meridional heat transport. Instead, the condensation flow onto the Olympus Mons and Tharsis Montes region syphoned away energy that may otherwise have been transported into the polar region. The generation of condensation flow in the martian atmosphere greatly influences the overall meridional transport of energy. Condensation flow was not accounted for in the previous EBM simulations, which explains the different range of atmospheric collapse predicted by our simulations and by previous EBM simulations.

Acknowledgments

References

Aharonson, O., Zuber, M.T., Neumann, G.A., Head, J.W., 1998. Mars: Northern hemisphere slopes and slope distributions. Geophys. Res. Lett. 25, 4413–4416.

Andrews, D.G., Holton, J.R., Leovy, C.B., 1987. Middle Atmosphere Dynamics. Academic press.

Andrews-Hanna, J.C., Lewis, K.W., 2011. Early Mars hydrology: 2. Hydrological evolution in the Noachian and Hesperian epochs. J. Geophys. Res. 116 (E2).

Carr, M.H., Head, J.W., 2010. Geologic history of Mars. Earth Planet. Sci. Lett. 294 (3–4), 185–203.

Christensen, P.R. et al., 2001. Mars Global Surveyor Thermal Emission Spectrometer experiment: Investigation description and surface science results. J. Geophys. Res. 106, 23823–23872.

Colaprete, A., Toon, O.B., 2003. Carbon dioxide clouds in an early dense Martian atmosphere. J. Geophys. Res. 108 (E4), 6-1–6-23. http://dx.doi.org/10.1029/2002JE001967, 5025.

Davies, D.W., 1979. Effects of dust on the heating of Mars' surface and atmosphere. J. Geophys. Res. 84 (B14), 8289–8293.

Ehlmann, B.L. et al., 2011. Subsurface water and clay mineral formation during the early history of Mars. Nature 479 (7371), 53–60.

Fassett, C.I., Head, J.W., 2011. Sequence and timing of conditions on early Mars. Icarus 211 (2), 1204–1214.

Forget, F., Pierrehumbert, R.T., 1997. Warming early Mars with carbon dioxide clouds that scatter infrared radiation. Science 278 (5341), 1273–1276.

Forget, F., Wordsworth, R., Millour, E., Madeleine, J.-B., Kerber, L., Leconte, J., Marcq, E., Haberle, R., 2013. 3d modelling of the early martian climate under a denser CO_2 atmosphere: Temperatures and CO_2 ice clouds. Icarus 222 (1), 81–99, <http://www.sciencedirect.com/science/article/pii/S0019103512004265>.

Gierasch, P.J., Toon, O.B., 1973. Atmospheric pressure variation and the climate of Mars. J. Atmos. Sci. 30 (8), 1502–1508.

Gilliland, R.L., 1989. Solar evolution. Palaeogeogr. Palaeoclimatol. Palaeoecol. 75 (1–2), 35–55.

Glasser, L., 2002. Equations of state and phase diagrams. J. Chem. Educ. 79 (7), 874–876.

Goody, R.M., Yung, Y.L., 1989. Atmospheric Radiation: Theoretical Basis. Oxford University Press.

Gough, D.O., 1981. Solar interior structure and luminosity variations. Sol. Phys. 74, 21–34.

Grotzinger, J.P. et al., 2005. Stratigraphy and sedimentology of a dry to wet eolian depositional system, Burns formation, Meridiani Planum, Mars. Earth Planet. Sci. Lett. 240, 11–72.

Guo, X., Richardson, M.I., Soto, A., Toigo, A., 2010. On the mystery of the perennial carbon dioxide cap at the south pole of Mars. J. Geophys. Res. 115, E04005. http://dx.doi.org/10.1029/2009JE003382.

Haberle, R.M., Leovy, C.B., Pollack, J.B., 1982. Some effects of global dust storms on the atmospheric circulation of Mars. Icarus 50 (2–3), 322–367.

Haberle, R.M. et al., 1993. Mars atmospheric dynamics as simulated by the NASA Ames general circulation model: 1. The zonal-mean circulation. J. Geophys. Res.: Planets 98 (E2), 3093–3123. http://dx.doi.org/10.1029/92JE02946.

Haberle, R.M., Tyler, D., McKay, C.P., Davis, W.L., 1994. A model for the evolution of CO_2 on Mars. Icarus 109, 102–120.

Halevy, I., Pierrehumbert, R.T., Schrag, D.P., 2009. Radiative transfer in CO_2-rich paleoatmospheres. J. Geophys. Res.: Atmos. 114 (D18), 2156–2202.

Head, J.W., Mustard, J.F., Kreslavsky, M.A., Milliken, R.E., Marchant, D.R., 2003. Recent ice ages on Mars. Nature 426, 797–802.

Hess, S.L., Henry, R.M., Tillman, J.E., 1979. The seasonal variation of atmospheric pressure on Mars as affected by the south polar cap. J. Geophys. Res. 84 (B6), 2923–2927.

Hess, S.L., Ryan, J.A., Tillman, J.E., Henry, R.M., Leovy, C.B., 1980. The annual cycle of pressure on Mars measured by Viking Landers 1 and 2. Geophys. Res. Lett. 7 (3), 197–200.

Kahre, M.A., Vines, S.K., Haberle, R.M., Hollingsworth, J.L., 2013. The early martian atmosphere: Investigating the role of the dust cycle in the possible maintenance of two stable climate states. J. Geophys. Res.: Planets. http://dx.doi.org/10.1002/jgre.20099.

Kieffer, H., 1979. Mars south polar spring and summer temperatures: A residual CO_2 frost. J. Geophys. Res. 84 (B14), 8263–8828.

Kieffer, H.H., 2007. Cold jets in the martian polar caps. J. Geophys. Res. 112 (E08005).

Kieffer, H.H., Martin, T.Z., Peterfreund, A.R., Jakosky, B.M., Miner, E.D., Palluconi, F.D., 1977. Thermal and albedo mapping of Mars during the viking primary mission. J. Geophys. Res. 82 (28), 4249–4291.

Kreslavsky, M.A., Head, J.W., 2005. Mars at very low obliquity: Atmospheric collapse and the fate of volatiles. Geophys. Res. Lett. 32, L12202.

Laprise, R., 1992. The euler equations of motion with hydrostatic pressure as an independent variable. Mon. Weather Rev. 120 (1), 197–207. http://dx.doi.org/10.1175/1520-0493(1992)120<0197:TEEOMW>2.0.CO;2.

Laskar, J., Correia, A.C.M., Gastineau, M., Joutel, F., Levrard, B., Robutel, P., 2004. Long term evolution and chaotic diffusion of the insolation quantities of Mars. Icarus 170, 343–364.

Leighton, R.R., Murray, B.C., 1966. Behavior of carbon dioxide and other volatiles on Mars. Science 153, 136–144.

Leovy, C., Mintz, Y., 1969. Numerical simulation of the atmospheric circulation and climate of Mars. J. Atmos. Sci. 26 (6), 1167–1190. http://dx.doi.org/10.1175/1520-0469(1969)026<1167:NSOTAC>2.0.CO;2.

Lindzen, R.S., Farrell, B., 1977. Some realistic modifications of simple climate models. J. Atmos. Sci. 34 (10), 1487–1501.

Lindzen, R.S., Farrell, B., 1980. The role of polar regions in global climate, and a new parameterization of global heat transport. Mon. Weather Rev. 108 (12), 2064–2079.

Manning, C.V., McKay, C.P., Zahnle, K.J., 2006. Thick and thin models of the evolution of carbon dioxide on Mars. Icarus 180, 38–59.

McKay, C.P., Toon, O.B., Kasting, J.F., 1991. Making Mars habitable. Nature 352 (6335), 489–496.

Mellon, M.T., 1996. Limits on the CO_2 content of the martian polar deposits. Icarus 124 (1), 268–279.

Mischna, M.A., Kasting, J.F., Pavlov, A., Freedman, R., 2000. Influence of carbon dioxide clouds on early martian climate. Icarus 145 (2), 546–554.

Mischna, M.A., Lee, C., Richardson, M., 2012. Development of a fast, accurate radiative transfer model for the martian atmosphere, past and present. J. Geophys. Res. 117, E10009.

Mischna, M.A., Baker, V., Milliken, R., Richardson, M., Lee, C., 2013. Effects of obliquity and water vapor/trace gas greenhouses in the early martian climate. J. Geophys. Res.: Planets 118. http://dx.doi.org/10.1002/jgre.20054.

Nakamura, T., Tajika, E., 2002. Stability of the martian climate system under the seasonal change condition of solar radiation. J. Geophys. Res. 107 (E11).

Nye, J.F., Durham, W.B., Schenk, P.M., Moore, J.M., 2000. The instability of a south polar cap on Mars composed of carbon dioxide. Icarus 144, 449–455.

Peixoto, J., Oort, A., 1992. Physics of Climate. American Institute of Physics.

Perrin, M., Hartmann, J., 1989. Temperature-dependent measurements and modeling of absorption by CO_2–N_2 mixtures in the far line-wings of the 4.3 m {CO_2} band. J. Quant. Spectrosc. Radiat. Transfer 42 (4), 311–317, <http://www.sciencedirect.com/science/article/pii/0022407389900770>.

Pierrehumbert, R.T., 2010. Principles of Planetary Climate. Cambridge University Press, Cambridge, UK.

Pollack, J.B., Leovy, C.B., Greiman, P.W., Mintz, Y., 1981. A martian general circulation experiment with large topography. J. Atmos. Sci. 38 (1), 3–29, 2011/11/08.

Pollack, J.B., Haberle, R.M., Schaeffer, J., Lee, H., 1990. Simulations of the general circulation of the martian atmosphere 1. Polar processes. J. Geophys. Res. 95 (B2), 1447–1473.

Putzig, N.E., Mellon, M.T., Kretke, K.A., Arvidson, R.E., 2005. Global thermal inertia and surface properties of Mars from the MGS mapping mission. Icarus 173 (2), 325–341.

Reynolds, O., 1895. On the dynamical theory of incompressible viscous fluids and the determination of the criterion. Philos. Trans. Roy. Soc. London. A, 123–164.

Richardson, M., Toigo, A., Newman, C., 2007. Planetwrf: A general purpose, local to global numerical model for planetary atmospheric and climate dynamics. J. Geophys. Res. 112, E09001.

Skamarock, W.C. et al., 2005. A Description of the Advanced Research WRF Version 2. NCAR Tech Note NCAR/TN-468+STR.

Skamarock, W.C. et al., 2008. A Description of the Advanced Research WRF Version 3. NCAR Tech Note NCAR/TN-468+STR.

Smith, D.E. et al., 2001. Mars orbiter laser altimeter: Experiment summary after the first year of global mapping of Mars. J. Geophys. Res. 106, 23689–23722.

Stone, P.H., 1972. A simplified radiative-dynamical model for the static stability of rotating atmospheres. J. Atmos. Sci. 29 (3), 405–418.

Tillman, J.E., Johnson, N.C., Guttorp, P., Percival, D.B., 1993. The martian annual atmospheric pressure cycle: Years without great dust storms. J. Geophys. Res. 98 (E6), 10963–10971.

Toigo, A.D., Lee, C., Newman, C.E., Richardson, M.I., 2012. The impact of resolution on the dynamics of the martian global atmosphere: Varying resolution studies with the MarsWRF GCM. Icarus 221, 276–288.

Toon, O.B., Pollack, J.B., Ward, W., Burns, J.A., Bilski, K., 1980. The astronomical theory of climatic change on Mars. Icarus 44 (3), 552–607.

Urata, R.A., Toon, O.B., 2013. Simulations of the martian hydrologic cycle with a general circulation model: Implications for the ancient martian climate. Icarus 226 (1), 229–250.

Ward, W.R., 1974. Climatic variations on Mars 1. Astronomical theory of insolation. J. Geophys. Res. 79 (24), 3375–3386.

Wood, S.E., Paige, D.A., 1992. Modeling the martian seasonal CO_2 cycle. I. Fitting the Viking Lander pressure curves. II. Interannual variability. Icarus 99, 1–27.

Wordsworth, R., Forget, F., Eymet, V., 2010. Infrared collision-induced and far-line absorption in dense CO_2 atmospheres. Icarus 210 (2), 992–997.

Wordsworth, R., Forget, F., Millour, E., Head, J.W., Madeleine, J.-B., Charnay, B., 2013. Global modelling of the early martian climate under a denser CO_2 atmosphere: Water cycle and ice evolution. Icarus 222, 1–19.